Redox-controlled structural reorganization and flavin strain within the ribonucleotide reductase R2b-NrdI complex monitored by serial femtosecond crystallography

Juliane John[1], Oskar Aurelius[1,2], Vivek Srinivas[1], In-Sik Kim[3], Asmit Bhowmick[3], Philipp S. Simon[3], Medhanjali Dasgupta[3], Cindy Pham[3], Sheraz Gul[3], Kyle D. Sutherlin[3], Pierre Aller[4,5], Agata Butryn[4,5,6], Allen M. Orville[4,5], Mun Hon Cheah[7], Shigeki Owada[8,9], Kensuke Tono[8,9], Franklin D. Fuller[10], Alexander Batyuk[10], Aaron S. Brewster[3], Nicholas K. Sauter[3], Vittal K. Yachandra[3], Junko Yano[3], Jan Kern[3]*, Hugo Lebrette[1,11]* & Martin Högbom[1]*

[1]Department of Biochemistry and Biophysics, Stockholm University, Arrhenius Laboratories for Natural Sciences, Stockholm, Sweden
[2]MAX IV Laboratory, Lund University, Lund, Sweden
[3]Molecular Biophysics and Integrated Bioimaging Division, Lawrence Berkeley National Laboratory, Berkeley, CA, USA
[4]Diamond Light Source Ltd, Harwell Science and Innovation Campus, Didcot, UK
[5]Research Complex at Harwell, Harwell Science and Innovation Campus, OX11 0FA, Didcot, UK
[6]Present address: Macromolecular Machines Laboratory, The Francis Crick Institute, London NW1 1AT, UK
[7]Department of Chemistry - Ångström, Molecular Biomimetics, Uppsala University, SE 751 20 Uppsala, Sweden
[8]Japan Synchrotron Radiation Research Institute, 1-1-1 Kouto, Sayo-cho, Sayo-gun, Hyogo, 679-5198, Japan
[9]RIKEN SPring-8 Center, 1-1-1 Kouto, Sayo-cho, Sayo-gun, Hyogo, 679-5148, Japan
[10]LCLS, SLAC National Accelerator Laboratory, Menlo Park, CA, USA
[11]Present address: Laboratoire de Microbiologie et Génétique Moléculaires (LMGM), Centre de Biologie Intégrative (CBI), CNRS, UPS, Université de Toulouse, Toulouse, France

*Corresponding authors: jfkern@lbl.gov, hugo.lebrette@dbb.su.se, hogbom@dbb.su.se

Abstract

Redox reactions are central to biochemistry and are both controlled by and induce protein structural changes. Here we describe structural rearrangements and crosstalk within the *Bacillus cereus* ribonucleotide reductase R2b-NrdI complex, a di-metal carboxylate-flavoprotein system, as part of the mechanism generating the essential catalytic free radical of the enzyme. Femtosecond crystallography at an X-ray free-electron laser was utilized to obtain structures at room temperature in defined redox states without suffering photoreduction. We show that the flavin in the hydroquinone state is under steric strain in the R2b-NrdI protein complex, presumably tuning its redox potential to promote superoxide generation. Moreover, a binding site in close vicinity to the expected flavin O_2-interacton site is observed to be controlled by the redox state of the flavin and linked to the channel proposed to funnel the produced superoxide species from NrdI to the di-manganese site in protein R2b. These specific features are coupled to further structural changes around the R2b-NrdI interaction surface. The mechanistic implications for the control of reactive oxygen species and radical generation in protein R2b are discussed.

Introduction

Ribonucleotide reductases (RNRs) are essential metalloenzymes that employ sophisticated radical chemistry to reduce the 2'-OH group of ribonucleotides and thereby produce deoxyribonucleotides (dNTPs), the building blocks of DNA. This reaction is the only known pathway for the *de novo* synthesis of dNTPs. Three classes of RNRs are differentiated based on their structural features and radical generating mechanism. Class I consists of a radical generating subunit, R2 and a catalytic subunit, R1. Oxygen is required to generate a radical in the R2 subunit, which is reversibly shuttled to R1 to initiate the ribonucleotide reduction. Class I, found in eubacteria and all eukaryotes, is to date divided into five subclasses, Ia – Ie, based on the type of metal cofactor, metal ligands and radical storage in R2 (Högbom et al., 2020). The R2 subunit is characterized by a ferritin-like fold housing two metal ions coordinated by six conserved residues (Nordlund & Reichard, 2006), i.e. two histidines and four carboxylates (with the exception of subclass Ie (Blaesi et al., 2018; Srinivas et al., 2018)). The class Ib R2 subunit (R2b) metal site can bind two manganese ions or two iron ions. The two metal ions are oxidized from the M(II)/M(II) state to a short-lived M(III)/M(IV) intermediate which decays to M(III)/M(III) while producing a radical species on an adjacent tyrosyl residue (Tyr·), where it is also stored (Cotruvo et al., 2013; Cotruvo & Stubbe, 2010). The di-manganese R2b was shown to be the physiologically relevant form of R2b (Cotruvo & Stubbe, 2010; Cox et al., 2010); it accumulates higher amounts of radical and has higher enzymatic activity than the di-iron R2b. Molecular oxygen (O_2) can directly activate the di-iron R2b (Huque et al., 2000). In contrast, the di-manganese R2b form cannot react with O_2 but requires a superoxide radical ($O_2^{\bullet-}$) provided by NrdI, a flavoprotein which is generally

encoded in the same operon as R2b (Berggren et al., 2014; Cotruvo & Stubbe, 2010; Roca et al., 2008).

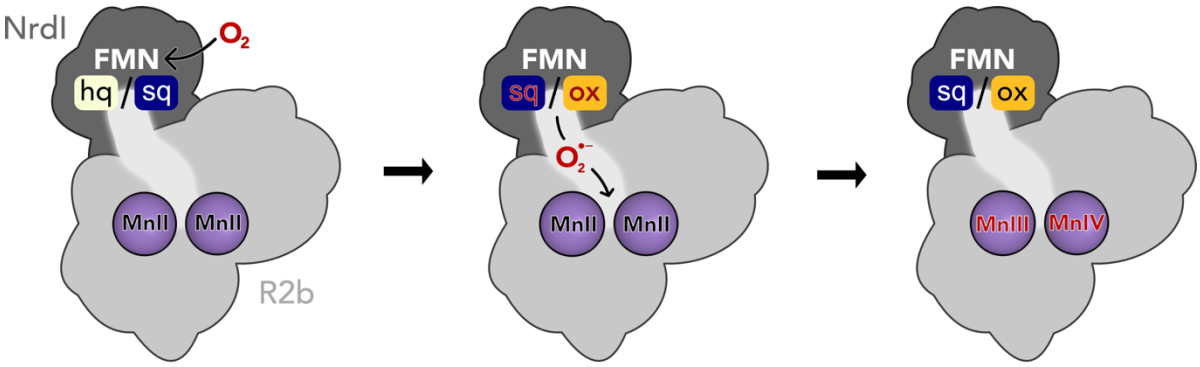

Scheme 1 **Activation of the di-manganese centre in ribonucleotide reductase class Ib R2**. Both hydroquinone (hq) and semiquinone (sq) FMN of NrdI can reduce molecular oxygen to superoxide, which is shuttled to the metal site in R2b and activates the di-manganese cofactor. FMN is oxidized either to semiquinone or the fully oxidized form (ox) in the process.

NrdI is a small, globular protein that binds the redox-active flavin mononucleotide (FMN) cofactor. NrdI stands out in comparison to other flavodoxins, which perform single one- or two-electron transfers, by being able to perform two successive one-electron reductions (Cotruvo & Stubbe, 2008, 2010). Fully reduced NrdI with hydroquinone FMN ($NrdI_{hq}$) can reduce O_2 to $O_2^{\bullet-}$ while being oxidized to semiquinone NrdI ($NrdI_{sq}$) (Cotruvo et al., 2013). $NrdI_{sq}$ can in turn produce a second $O_2^{\bullet-}$ from another O_2 molecule and become fully oxidized ($NrdI_{ox}$) in the process (Berggren et al., 2014). The oxidation state of NrdI can be followed by ultraviolet–visible light absorption (UV–vis) spectroscopy. NrdI is faint yellow in the hydroquinone state, dark blue in the semiquinone state and bright orange in the oxidized state (Røhr et al., 2010) (Fig. S1). NrdI binds tightly to R2b in a 1:1 ratio with FMN at the protein–protein interface, forming a dimer of heterodimers. Previously obtained crystal structures of the R2b-NrdI complex from *Escherichia coli* and *Bacillus cereus* show that a

89 conserved channel connects FMN and the metal site in R2b (Boal et al., 2010; Hammerstad et
90 al., 2014). This channel is proposed to shuttle $O_2^{\bullet-}$ produced by NrdI in complex with R2b to
91 the metal site, where the radical is formed. Here we investigate the structural details and
92 reaction mechanism of the activation of NrdI by O_2 as well as the subsequent shuttling of $O_2^{\bullet-}$
93 to the metal site for the generation of Tyr· in R2b.
94
95 Studying structural changes in redox-active proteins is challenging from an experimental point
96 of view. X-ray crystallography is a well-suited method for investigating both high-resolution
97 structural details in the redox-active centres as well as overall reorganization of proteins.
98 However, both metalloenzymes and flavodoxins are very sensitive to photoreduction during
99 the exposure to the high-energy X-ray radiation of synchrotron sources. Synchrotron crystal
100 structures of RNR and NrdI proteins invariably suffer from photoreduction, which complicates
101 the determination of the oxidation state of redox active centres and has proven to be a
102 problem for obtaining fully oxidized structures (Grāve et al., 2019; Johansson et al., 2010;
103 Røhr et al., 2010). While there are well established experimental workarounds like short
104 exposure times, helical data collection and serial synchrotron crystallography the time-scales
105 necessary to obtain the diffraction data using these methods cannot fully avoid the reducing
106 effects of the X-ray radiation (Spence, 2017). Serial femtosecond crystallography (SFX)
107 overcomes this problem by the so-called diffraction-before-destruction principle (Doerr,
108 2011; Nass, 2019; Neutze et al., 2000). Short intense X-ray pulses of the duration of only a
109 few femtoseconds are produced by an X-ray free electron laser (XFEL), illuminating one crystal
110 and giving rise to one diffraction pattern at a time. The crystal is generally destroyed in the
111 process and needs to be replaced by a new one for the next image. This method allows to

112 record the scattering information before atomic displacement has time to occur resulting in
113 a dataset effectively free from the effects of radiation damage (Spence, 2017).
114
115 Here we present the first SFX structures of R2b in complex with NrdI in the oxidized and
116 hydroquinone state. The datasets reveal redox-dependent structural rearrangements both in
117 the FMN binding pocket of NrdI and at the protein interface. Despite the significant
118 rearrangement in the direct vicinity of the cofactor, FMN itself changes surprisingly little
119 between redox states. This marks an interesting contrast to structures of free NrdI, which
120 display significant conformational change of FMN between different oxidation states. We
121 conclude that the R2b-NrdI complex formation is restricting FMN movement and inhibits this
122 conformational change with implications for its redox potential and O_2 reactivity. We also
123 describe the first R2b-NrdI complex with a di-manganese metal centre from *Bacillus cereus*.
124 The metal coordination in both structures blocks access to the channel that connects FMN
125 and the metal site providing further information on gating and control of catalytic reactive
126 oxygen species.

Results

SFX crystal structures of *Bacillus cereus* R2b in complex with oxidized and hydroquinone NrdI collected at ambient temperature

An initial crystallization condition for the R2b-NrdI complex was optimized to yield a sufficient amount of crystals smaller than 100 µm in the longest axis (Fig. S1), the maximum acceptable crystal size for the experimental setup. Crystals were initially tested at SACLA (SPring-8 Angstrom Compact free electron LAser, Japan) under aerobic conditions with a grease extruder setup (data not shown) (Sugahara et al., 2015; Tono et al., 2013). The crystals diffracted to 2 Å and proved to be stable under room temperature for several days and sturdy enough to handle the physical stress of being manipulated for the experiment. At LCLS (Linac Coherent Light Source at SLAC National Accelerator Laboratory, USA), we obtained two structures of the *Bacillus cereus* R2b-NrdI (*Bc*R2b-NrdI) complex in different defined redox states by SFX. The datasets were collected at room temperature under anaerobic conditions using the drop-on-demand sample delivery method (Fuller et al., 2017) (see Materials and Methods for details).

*Bc*R2b protein was produced metal-free to allow full control over metal loading during complex reconstitution. The metal content of the protein was determined by total-reflection X-ray fluorescence (TXRF) and only trace amounts of metals could be detected. The iron and manganese content per R2b monomer corresponded to metal-to-protein molar ratios of 0.27 ± 0.04%, and 0.07 ± 0.04%, respectively. The *Bc*R2b-NrdI complex was reconstituted *in vitro*

by mixing both proteins in a molar ratio of 1:1 and set up for batch crystallization. Manganese was present both during the complex reconstitution and in the crystallization condition. Crystals for two different datasets were prepared to investigate different oxidation states of NrdI. The crystals for the first dataset were grown under aerobic conditions, yielding bright orange crystals, indicating that NrdI was fully oxidized (Fig. S1). The structure from these crystals is later referred to as *Bc*R2b$_{MnMn}$-NrdI$_{ox}$ (PDB ID: 7Z3D). The second dataset was obtained by reducing *Bc*R2b$_{MnMn}$-NrdI$_{ox}$ crystals chemically with sodium dithionite in an anaerobic environment. Consequently, the crystal colour changed from bright orange to faint yellow, indicating that NrdI underwent a two-electron reduction to the hydroquinone state (Fig. S1). The crystals were subsequently kept under anaerobic conditions, preventing reoxidation of NrdI. The corresponding structure is denoted *Bc*R2b$_{MnMn}$-NrdI$_{hq}$ (PDB ID: 7Z3E).

Overall structure

The two structures were solved in space group $C222_1$ and are of very similar quality with a resolution of 2.0 Å and similar unit cell dimensions (Table 1). The asymmetric unit contains one monomer of the 1:1 *Bc*R2b-NrdI complex. The physiological dimer can be generated by applying crystal symmetry (Fig. 1 A). Clear electron density maps allowed us to model residues 1-299 of 322 for R2b and 1-116 of 118 for NrdI in *Bc*R2b$_{MnMn}$-NrdI$_{ox}$ and 1-298 of R2b and all 118 residues of NrdI in *Bc*R2b$_{MnMn}$-NrdI$_{hq}$. Overall *Bc*R2b$_{MnMn}$-NrdI$_{ox}$ and *Bc*R2b$_{MnMn}$-NrdI$_{hq}$ are similar, as indicated by the Cα root-mean-square deviation (RMSD) value of 0.16 Å (Fig. 1 B). Refinement of both structures was conducted independently from each other following the same protocol (see Materials and Methods for details) with final R_{work}/R_{free} of 0.16/0.20 for *Bc*R2b$_{MnMn}$-NrdI$_{ox}$ and 0.15/0.18 for *Bc*R2b$_{MnMn}$-NrdI$_{hq}$ (Table 1). Hammerstad *et al.* previously

reported two crystal structures of the *Bc*R2b-NrdI complex (Hammerstad et al., 2014), obtained by single-crystal X-ray diffraction at a synchrotron source and under cryogenic conditions. Here, however, R2b harbours a di-iron active site. These structures will be referred to as *Bc*R2b$_{FeFe}$-NrdI-1 and *Bc*R2b$_{FeFe}$-NrdI-2 (PDB ID: 4BMO and 4BMP, respectively). Structural alignment between the published synchrotron and our XFEL structures shows that the overall fold of the complex is similar with Cα-RMSD values between 0.42 and 0.47 Å (Fig. 1 B). Compared to the *Bc*R2b$_{FeFe}$-NrdI structures we observe a 7-8 residue extended ordered C-terminus in our structures. The C-terminus in *Bc*R2b$_{MnMn}$-NrdI$_{ox}$ continues in the same orientation as the C-terminal α-helix without keeping a helical conformation. It interacts with a groove between R2b and NrdI extending the R2b-NrdI binding area by forming hydrogen bonds to two other α-helices of R2b and a loop in NrdI (Fig. S2).

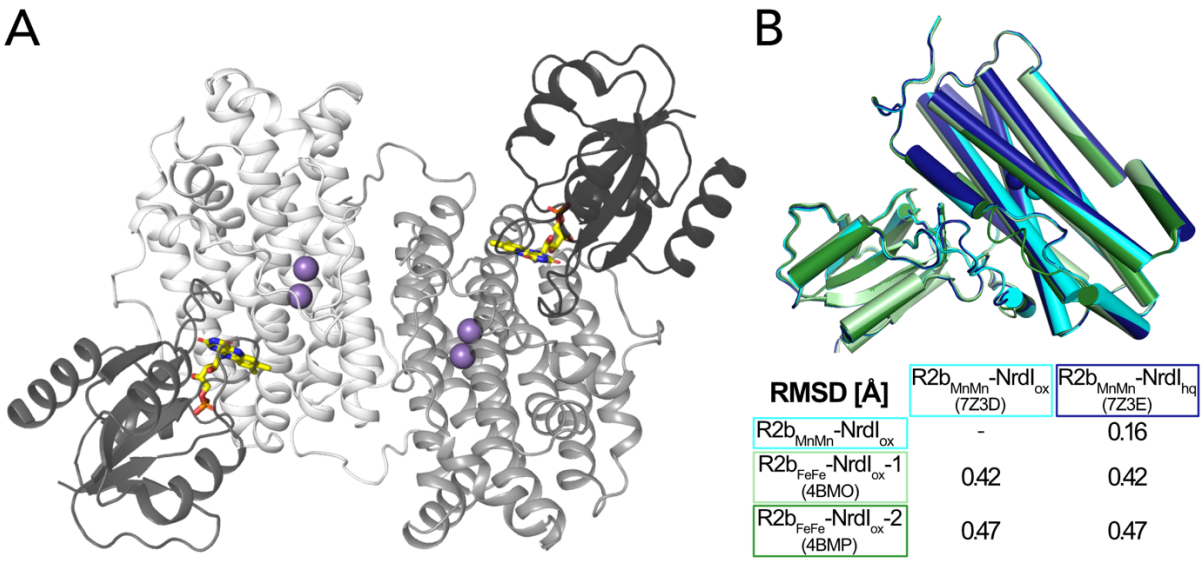

RMSD [Å]	R2b$_{MnMn}$-NrdI$_{ox}$ (7Z3D)	R2b$_{MnMn}$-NrdI$_{hq}$ (7Z3E)
R2b$_{MnMn}$-NrdI$_{ox}$	-	0.16
R2b$_{FeFe}$-NrdI$_{ox}$-1 (4BMO)	0.42	0.42
R2b$_{FeFe}$-NrdI$_{ox}$-2 (4BMP)	0.47	0.47

Figure 1 A) **Structure of the *Bc*R2b-NrdI complex** (PDB ID: 7Z3D). In each 1:1 R2b-NrdI dimer, R2b and NrdI are coloured in lighter and darker grey, respectively. The second dimer is generated by crystal symmetry. Manganese ions are represented as purple spheres and FMN as yellow sticks at the R2b-NrdI interface. B) Superimposition of all structures of the *Bc*R2b-NrdI dimer with their corresponding Cα RMSD in the table. Individual structures are colour coded identically in the figure and the table.

192 Table 1 Data collection and refinement statistics. Values in parenthesis are for the highest resolution shell.

	***Bc*R2b$_{MnMn}$-NrdI$_{ox}$**	***Bc*R2b$_{MnMn}$-NrdI$_{hq}$**
PDB ID	7Z3D	7Z3E
Data collection statistics		
XFEL source	LCLS MFX	LCLS MFX
Wavelength (Å)	1.30	1.30
Space group	$C222_1$	$C222_1$
Unit cell dimensions a, b, c (Å)	61.4, 125.6, 145.0	61.2, 125.8, 144.8
Unit cell angles α, β, γ (°)	90, 90, 90	90, 90, 90
Resolution range (Å)	51.59 - 2.0 (2.034 - 2.0)	51.47 - 2.0 (2.034 - 2.0)
Unique reflections	38319 (1881)	38188 (1880)
Multiplicity	66.94 (25.42)	59.92 (26.46)
Merged lattices	14357	13509
Completeness (%)	99.91 (100)	99.91 (100)
Mean I/sigma (I)	3.247 (0.654)	3.28 (0.791)
Wilson B-factor (Å^2)	35.45	33.22
R_{split} (%)	11.1 (86.3)	11.1 (76.5)
$CC_{1/2}$	0.989 (0.32)	0.988 (0.39)
Refinement statistics		
Resolution range used in refinment (Å)	24.17 - 2.0 (2.07 - 2.0)	23.91 - 2.0 (2.07 - 2.0)
Reflections used in refinement	38253 (3745)	38119 (3729)
Reflections used for R_{free}	1909 (206)	1897 (203)
R_{work} (%)	15.91 (30.40)	15.16 (28.44)
R_{free} (%)	19.56 (32.27)	18.37 (31.18)
RMSD, bond distances (Å)	0.007	0.007
RMSD, bond angles (°)	0.79	0.81
Ramachandran favored (%)	99.27	98.79
Ramachandran allowed (%)	0.73	1.21
Ramachandran outliers (%)	0	0
Rotamer outliers (%)	0.79	1.05
Clashscore	1.86	2.58
Protein residues (R2b + NrdI)	415 (299 + 116)	416 (298 + 118)
Average B-factor (Å^2)	47.27	43.66
macromolecules	47.24	43.64
ligands	34.66	30.38
solvent	50.57	47.09
Number of non-H atoms	3655	3652
macromolecules	3462	3477
ligands	33	33
solvent	160	142

193

R2b complex formation prevents butterfly bend of FMN in NrdI

Three redox states of FMN are physiologically relevant for NrdI: oxidized (FMN_{ox}), neutral semiquinone (FMN_{sq}) and anionic hydroquinone (FMN_{hq}) (Cotruvo et al., 2013; Røhr et al., 2010) (Scheme 2). Reduction of free FMN causes the isoalloxazine to bend along the N5-N10 axis leading to a "bufferfly bend" where the isoalloxazine moiety deviates from planarity (Fig. 2 A) (Zheng & Ornstein, 1996).

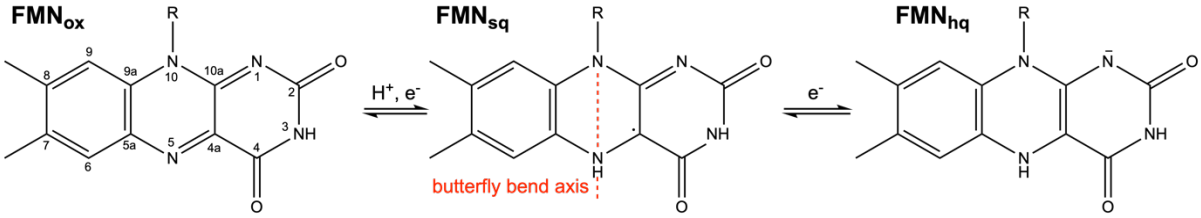

Scheme 2 **The physiologically relevant oxidation states of FMN in NrdI.** The red dashed line marks the virtual axis between N5 and N10. The ribityl phosphate group is denoted as R.

NrdI binds one molecule of FMN non-covalently. The pyrimidine ring of the 7,8-dimethyl-isoalloxazine ring is buried and tightly bound to the protein by a combination of hydrogen bonds and π-stacking interactions while the benzene ring and part of the phosphate tail are solvent exposed (Fig. 2 B). The crystal structure of *Bc*NrdI has been described previously by Røhr et. al and shows the FMN-binding pocket on the protein surface (Røhr et al., 2010). The same study also presents quantum mechanics/molecular mechanics (QM/MM) calculations of the theoretical butterfly bend for FMN bound to NrdI. The calculated angles are shallow with -3.1° for FMN_{ox} and -3.9° for FMN_{sq} and more pronounced with 14.1° for FMN_{hq} (Fig. 2 A). The authors investigated the influence of photoreduction on the butterfly bend in FMN bound to *Bc*NrdI. The crystals for the first structure (PDB ID: 2X2O, 1.1 Å resolution) were

produced from oxidized protein. The measured butterfly bend in this structure is 4.6° and does thus not correspond well to the calculated FMN_{ox} or FMN_{sq} angle. It does however resemble the calculated theoretical butterfly bend of 3.3° of the physiologically not relevant anionic semiquinone state of FMN (FMN_{sq-}) (Fig 2 A). The second NrdI structure (PDB ID: 2X2P, 1.2 Å resolution) structure was produced from protein in the semiquinone state and the butterfly bend was 11° after data collection, similar to the calculated FMN_{hq} angle (Fig. 2 A). The authors could confirm the reducing effect of the synchrotron radiation on FMN by comparing Raman spectra of the crystals before and after data collection. These structures will be referred to as *Bc*$NrdI_{ox+e}$ and *Bc*$NrdI_{sq+e}$ to emphasize the photoreduction. Johansson et al. observed the same discrepancy between the butterfly bend for a synchrotron structure of initially oxidized NrdI from *Bacillus anthracis* (*Ba*NrdI), a protein with 99% sequence identity to *Bc*NrdI and identical FMN protein environment (Johansson et al., 2010). *Ba*$NrdI_{ox+e}$ (PDB ID: 2XOD, 1.0 Å resolution) is even more bent than *Bc*$NrdI_{ox+e}$ with 5.7°, indicating significant photoreduction of FMN during data collection. Figure 2 A lists the FMN angles of the calculated and measured structures.

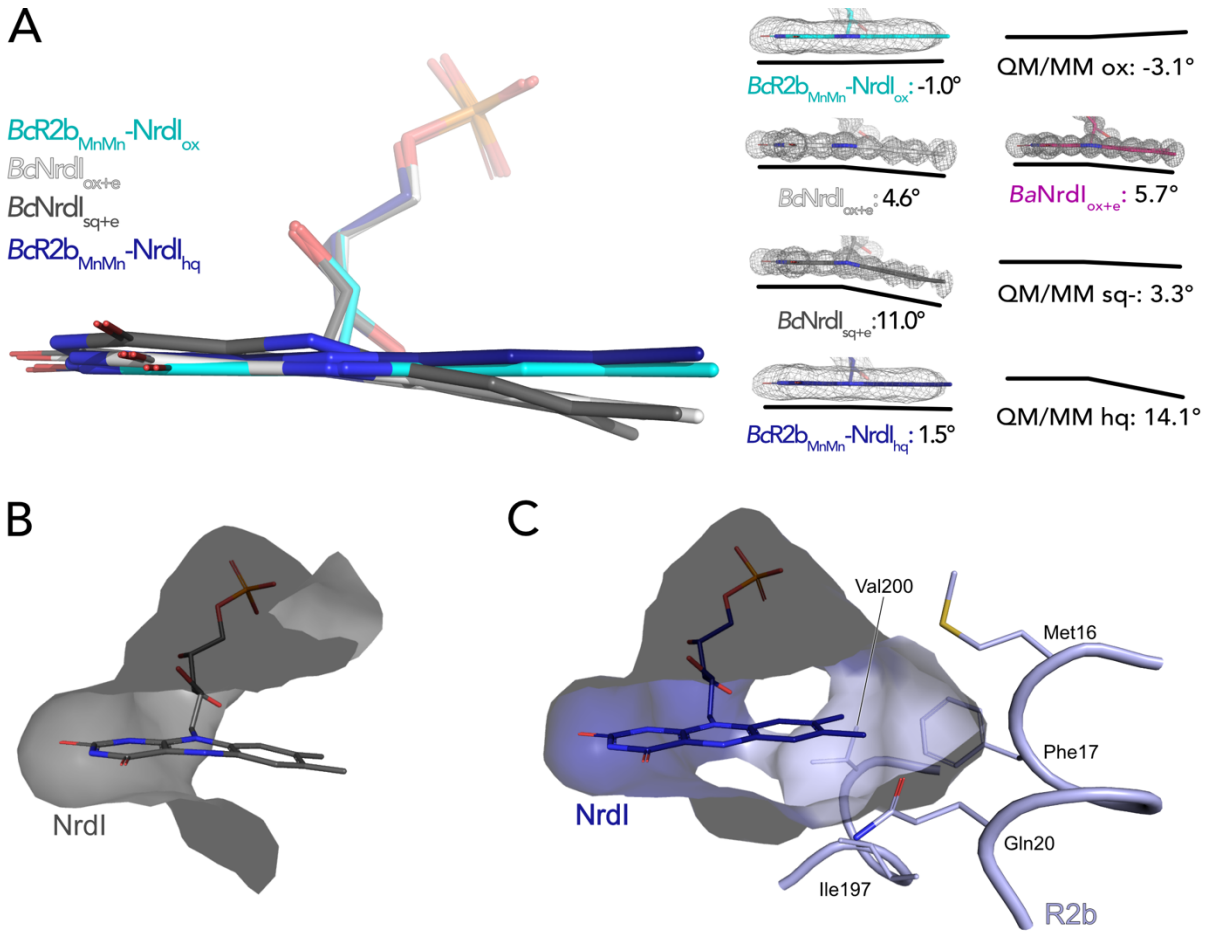

Figure 2 **The butterfly bending conformations of FMN in different redox states**. A) Left: Overlay of FMN cofactors of *B. cereus* NrdI in different crystal structures; Right: FMN cofactors in *Bc*NrdI and *Ba*NrdI with 2Fo-Fc maps contoured at 2 σ. Additionally, the theoretical calculated butterfly bend angles of FMN bound to *Bc*NrdI are shown (Røhr et al., 2010). Dark blue: *Bc*R2b$_{MnMn}$-NrdI$_{hq}$, cyan: *Bc*R2b$_{MnMn}$-NrdI$_{ox}$, grey: *Bc*NrdI$_{sq+e}$ (PDB ID: 2X2P), white: *Bc*NrdI$_{ox+e}$ (PDB ID: 2X2O), pink: *Ba*NrdI$_{ox+e}$(PDB ID: 2XOD). B) The benzene ring of FMN in *Bc*NrdI$_{sq+e}$ (PDB ID: 2X2P) is solvent exposed. C) In *Bc*R2b$_{MnMn}$-NrdI$_{hq}$ the FMN binding pocket is closed by residues contributed by R2b. Relevant residues are shown in sticks. The surface of the FMN binding pocket in NrdI in panels B) and C) is shown in grey.

The use of SFX allowed us, for the first time, to investigate the conformation of oxidized FMN in NrdI. In *Bc*R2b$_{MnMn}$-NrdI$_{ox}$, the isoalloxazine moiety of FMN$_{ox}$ is almost planar, with a butterfly bend of -1°. This value is comparable to the angle of -3.1° for FMN$_{ox}$ in NrdI calculated by QM/MM (Røhr et al., 2010). Unexpectedly, the bend of FMN$_{hq}$ in the *Bc*R2b$_{MnMn}$-

NrdI$_{hq}$ structure is minimal with only 1.5 ° and thus similar to FMN$_{ox}$ in the *Bc*R2b$_{MnMn}$-NrdI$_{ox}$ structure (Fig. 2 A). Additionally, we calculated an isomorphous difference (Fo(ox)-Fo(hq)) map of *Bc*R2b$_{MnMn}$-NrdI$_{ox}$ and *Bc*R2b$_{MnMn}$-NrdI$_{hq}$ using the phases of the oxidized dataset. These maps reduce model bias by directly comparing the experimental data and are very sensitive to subtle changes of atom positions in different data sets (Rould & Carter, 2003). The Fo(ox)-Fo(hq) map shows a slight movement of the oxygen on C4 of FMN indicating a small twist of the pyrimidine ring between both structures but no further bending (Fig. 3). This angle of *Bc*R2b$_{MnMn}$-NrdI$_{hq}$ does not correspond to either the calculated bend of FMN of 14.1° nor the experimental bending angle of *Bc*NrdI$_{sq+e}$ of 11°. In the R2b-NrdI complex the solvent exposed part of FMN is covered by R2b, which closes the binding pocket. The residues Met16 Phe17, Ile197 and Val200 of the R2b subunit interact hydrophobically with the benzene ring, while Gln20 is sterically hindering it from bending (Fig. 2 C). Together they form a rigid binding pocket for the isoalloxazine moiety of the cofactor, thereby preventing FMN$_{hq}$ from bending.

Reorganization of FMN environment and binding position controlled by FMN redox state

The change of redox state of FMN causes movement around the cofactor in both proteins. Alignment of the NrdI backbone of the *Bc*R2b$_{MnMn}$-NrdI$_{ox}$ and the *Bc*R2b$_{MnMn}$-NrdI$_{hq}$ structures shows a clear reorganization in the 40s loop close to the isoalloxazine ring of FMN (Fig. 3 A). The biggest change can be seen for Cα of Gly44 and a smaller shift for Cα of Thr43 and Phe45. The reorganization of the 40s loop of NrdI after reduction is also apparent in the superposition of both structures and in the Fo(ox)-Fo(hq) map (Fig. 3 B and C). Notably, Gly44 of NrdI is flipped by 180° and forms a hydrogen bond with the hydrogen of N5 on FMN. The hydrogen

bond between O4 of FMN and Gly46 shifts slightly. Thr43 in turn is shifted towards FMN and its side chain is rotated by 180°; Phe45 is also slightly rotated (Fig. 3 C). This redox-dependent conformational change of residues 43 to 45 was previously also observed in crystal structures of *Bc*NrdI and *Ba*NrdI in absence of the R2b subunit (PDB ID: 2X2O, 2X2P, 2XOD, 2XOE) (Johansson et al., 2010; Røhr et al., 2010).

Redox-induced changes are also visible on the side of the isoalloxazine ring facing R2b. An unknown molecule is bound within 5 Å from the reactive C4a of FMN in *Bc*R2b$_{MnMn}$-NrdI$_{ox}$, which binds O_2 to reduce it to $O_2^{\bullet-}$ (Ghisla & Massey, 1989). The molecule is 3- coordinated to Trp74 (NrdI), Ser196 (R2b) and a water (p-ox in Fig. 3 D and E). A similar density was previously observed in the di-iron *Bc*R2b-NrdI synchrotron structures where it was modelled as a chloride ion. In our structure, placing a water in this position does not sufficiently explain the density while modelling it as a chloride ion leaves no residual density (Fig. S3). Chloride is abundant in the crystallization condition; however, serine and tryptophane are not typical chloride ligands (Carugo, 2014). The exact nature of the molecule could not be determined and was thus left as a water in the final model. Interestingly, the binding position undergoes a redox dependent switch: In the reduced structure the density is instead found at a position between the oxygen on C2 of FMN$_{hq}$ and Asn71 of NrdI, 7 Å from the reactive C4a. Two adjacent water molecules make the unknown molecule 4-coordinated (p-hq in Fig. 3 D and E). To accommodate for the change of position residues Met77, Trp74, Asn71 and Glu98 from NrdI and Ser196 from R2b move in a plane parallel to the FMN isoalloxazine ring (Fig. 3 D and E). The unidentified molecule exchanges position with two different water molecules of the well-ordered solvent network connecting FMN with the active site in R2b. The solvent network is housed by a channel between both proteins lined by the side chains of Ser162,

Tyr166, Lys263 and Asn267 and the mainchain of Glu195 and Ser196 (Hammerstad et al., 2014). The position of the density in *Bc*R2b$_{MnMn}$-NrdI$_{ox}$ is close to the channel entrance on the R2b surface marked by Lys263, Asn267 and Ser196 (Fig. S4). Despite the large structural rearrangements around the FMN, the Fo(ox)-Fo(hq) map clearly shows that no redox-induced movement protrudes further down the channel and that the coordination of the metal site is unaffected by the change of NrdI redox state (Fig. 3 B and S4).

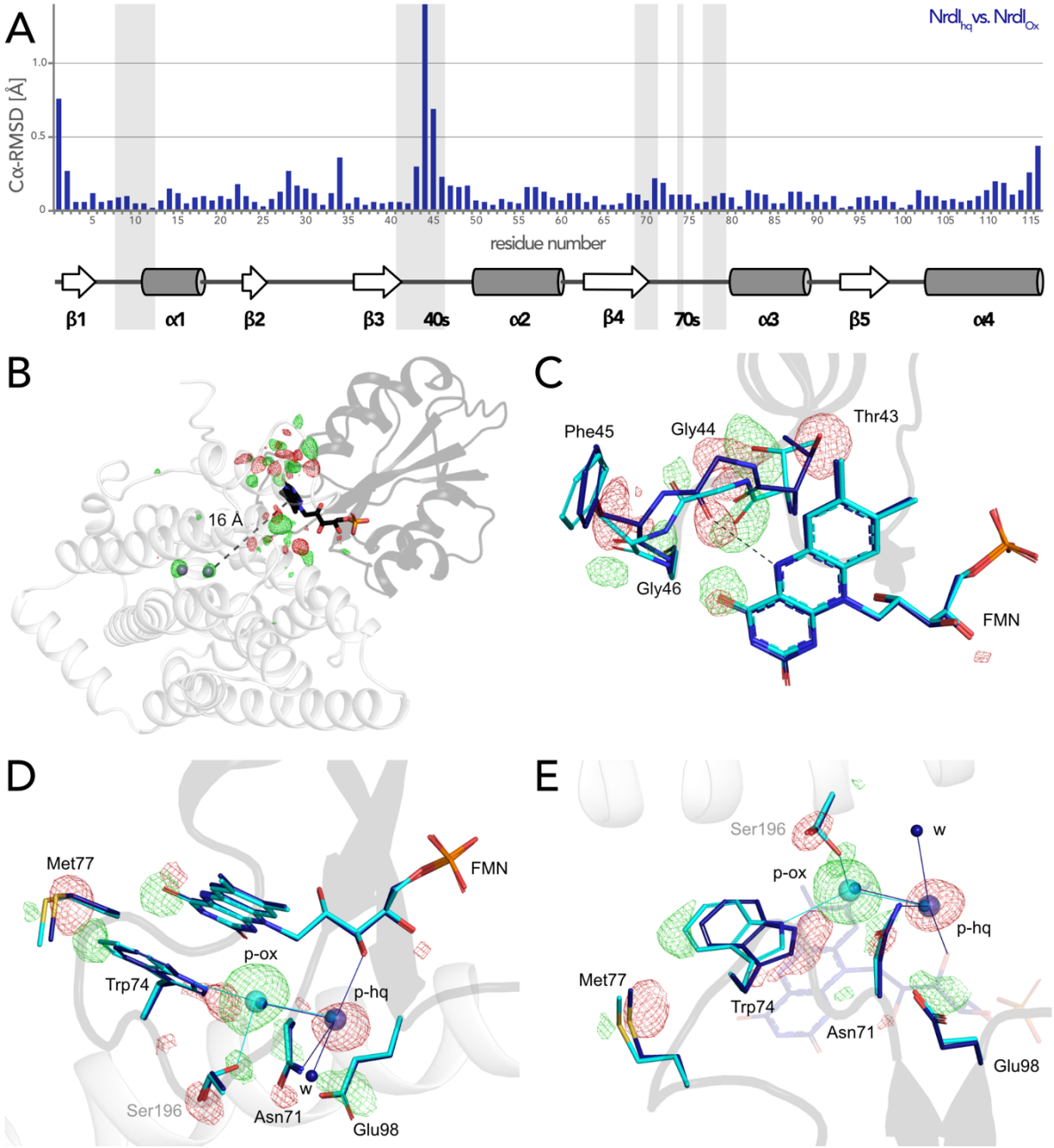

Figure 3 **FMN environment in the oxidized and hydroquinone *Bc*R2b-NrdI.** A) Structural alignment of NrdI in *Bc*R2b$_{MnMn}$-NrdI$_{ox}$ compared to *Bc*R2b$_{MnMn}$-NrdI$_{hq}$. Cα-RMSD in Å are shown for each residue of NrdI between the two models. The secondary structure assignment corresponding to the residues of NrdI is represented in the cartoon below. NrdI interactions with FMN are marked with light grey background B) Fo(ox)-Fo(hq) map contoured at 4.5 σ for the *Bc*R2b-NrdI complex with positive density in green and negative density in red. FMN are shown in sticks, manganese ions as purple spheres, R2b as transparent cartoon in white and NrdI in transparent black. Differences between both datasets cluster around the FMN at the R2b/NrdI interface. The distance between metal site and FMN is around 16 Å, marked with a dashed line. C) + D) + E) Close-ups of the

306 difference density around the FMN from different angles including superposition of *Bc*R2b$_{MnMn}$-NrdI$_{hq}$ in dark
307 blue and *Bc*R2b$_{MnMn}$-NrdI$_{ox}$ in cyan. Fo(ox)-Fo(hq) map contoured at 4.5 σ for all panels. Adjacent secondary
308 structure elements are shown as transparent cartoon in white for R2b and black for NrdI. C) Rearrangement of
309 the 40s loop of NrdI. Gly44 flips 180° in the hydroquinone state and forms a hydrogen bond with N5 of FMN
310 (shown as dashed line). D) Rearrangements of side chains on the R2b facing side of FMN. Residues of NrdI are
311 labelled in black, Ser196 from R2b in light grey. An unexplained density, larger than water, moves between the
312 structures, named p-ox and p-hq and is marked as transparent big spheres; waters are represented as small
313 opaque spheres. E) Same side chains as in D) are shown at a different angle facing the FMN. FMN is shown
314 transparent in the background for clarity.

315 Access to the metal site is not gated by FMN oxidation state, complex formation or
316 manganese binding

317

318 Both SFX *Bc*R2b-NrdI structures display a di-manganese metal centre with similar
319 coordination. In *Bc*R2b$_{MnMn}$-NrdI$_{ox}$ the two metal ions of R2b are refined at full occupancy and
320 the coordination sphere is clearly defined in the electron density map (Fig. 4 A). Mn1 is 4-
321 coordinated by His96, Glu93, Asp62 and Glu195. Mn2 is 5-coordinated by His198, Glu93,
322 Glu195 and Glu161. Notably, Glu195 and Glu161 exhibit two alternative conformations each
323 and alternately coordinate Mn2 in a monodentate or bidentate fashion. Importantly, while
324 Glu195 bridges the two ions, Glu161 coordinates only Mn2. No coordinating waters could be
325 identified (Fig. 4 B). The protein complex used in the crystallization for the *Bc*R2b$_{MnMn}$-NrdI$_{ox}$
326 dataset has not undergone any oxidation of the metal site and both manganese ions are in
327 the Mn(II)/Mn(II) oxidation state (see Materials and Methods and Discussion for details).
328 Notably, the reduction of FMN within NrdI occurs at about 16 Å from the metal site and does
329 not affect the metal coordination in *Bc*R2b-NrdI (Fig. 3 A). The Fo(ox)-Fo(hq) map shows
330 slightly lower occupancy for both manganese ions in *Bc*R2b$_{MnMn}$-NrdI$_{hq}$ (Fig S5). The loss of

metals can be explained by the reduction treatment of the crystals for this dataset and Mn1 was modelled with 80%, Mn2 with 90% occupancy in the reduced structure. Both structures show the same metal-metal distance of 3.8-3.9 Å within experimental error for this resolution (Fig. 4 B).

The metal-ligand Glu161 is likely a key player in the activation of the di-manganese centre as it is proposed to gate the access to the metal site for the oxidant produced by NrdI (Boal et al., 2010). Two main conformations have been observed for this ligand: In the "closed" conformation the glutamate interacts only with Mn2 and is proposed to prevent $O_2^{\bullet-}$ from reaching the metal site by obstructing the channel. In the "open" conformation, on the other hand, Glu161 bridges both manganese ions leaving space for three water molecules to connect Mn2 to the water network in the channel between FMN and the metal site. The open conformation of the equivalent glutamate has been observed in structures of di-manganese R2b alone, e.g. from *B. cereus*, *E. coli* and *Streptococcus sanguinis* (PDB ID: 4BMU, 3N37, 4N83) (Fig. 4 C) but also in the R2b-NrdI complex of *E. coli* (PDB ID: 3N3A) (Fig. 4 D) (Boal et al., 2010; Hammerstad et al., 2014; Makhlynets et al., 2014). Thus, NrdI binding to R2b is not responsible for triggering the open conformation of Glu161 (Glu158 in *E. coli* and Glu157 in *S. sanguinis*). It has been hypothesized that the presence of manganese ions in the active site could cause the glutamate to shift to the open conformation as the closed conformation is typically observed in R2b structures containing a di-iron site, e.g. in the *Bc*R2b$_{FeFe}$-NrdI complex (PDB ID: 4BMP) (Fig. 4 E) (Hammerstad et al., 2014). Indeed, since the di-iron form of R2b is oxidized by O_2 via a NrdI-independent pathway, the movement of the glutamate is not required for radical generation. However, our SFX *Bc*R2b$_{MnMn}$-NrdI structures harbour a di-manganese site and exhibit a Glu161 in the closed conformation, thereby demonstrating

that manganese in the active site is not sufficient to induce the glutamate shift. Finally, our radiation damage free structures also show that the opening of the channel towards the metal site is independent from the FMN oxidation state, as Glu161 is in the closed conformation when di-manganese R2b is in complex with either $NrdI_{ox}$ or $NrdI_{hq}$ (Fig. 4 B). Altogether, our data shows that the glutamate shift of Glu161 is not caused by the presence of manganese ions, R2b-NrdI complex formation, a specific NrdI redox state or a combination of these factors.

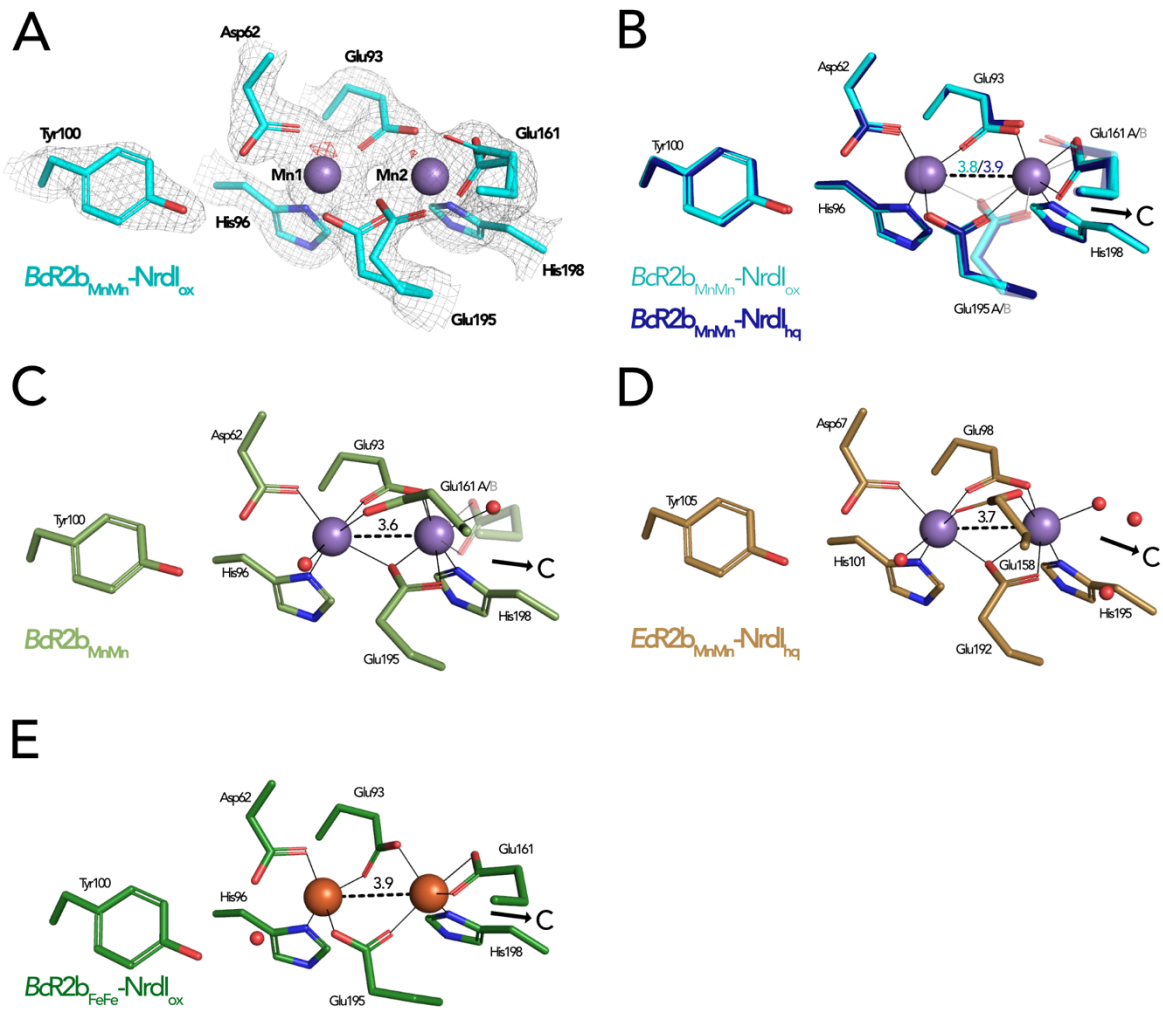

Figure 4 **Comparison of active site architecture in different R2b structures including the radical harbouring tyrosine.** Manganese ions are shown as purple, iron ions as orange and waters as red spheres. The direction of the connecting channel between R2b and NrdI is indicated by a black arrow and "C". A) *Bc*$R2b_{MnMn}$-$NrdI_{ox}$ active site. The 2Fo-Fc map is contoured at 2 σ shown as grey mesh and Fo-Fc is contoured at 4 σ with negative density

in red (no positive density is present). B) Superposition of *Bc*R2b$_{MnMn}$-NrdI$_{hq}$ and *Bc*R2b$_{MnMn}$-NrdI$_{ox}$. The metal coordination is identical for both structures. C) Active site of *Bc*R2b$_{MnMn}$ (PDB ID: 4BMU). The metal site of chain A is shown with Glu161 in both the open (opaque) and closed (transparent) conformation. D) Active site of *Ec*R2b$_{MnMn}$-NrdI$_{hq}$ (PDB ID: 3N3A). Glu158 is in the open conformation and two waters are in the position of the Glu161 of *Bc*R2b. E) Active site of the di-iron *Bc*R2b-NrdI complex (PDB ID: 4BMP). The metal coordination is similar to the manganese containing structures with Glu161 in the closed conformation. An additional water is hydrogen-bonded to Asp62 and Tyr100. Metal-metal distances are shown as dashed and metal ligands as solid lines; residues in alternative conformations are shown transparent for panels B)-E).

Discussion

In this study we present two structures of the manganese containing R2b-NrdI complex of *Bacillus cereus* with NrdI in two different oxidation states. These structures were obtained by room temperature SFX data collection using XFEL radiation in contrast to all previously studied R2b or NrdI structures, which were obtained by classical single-crystal synchrotron data collection at cryogenic temperatures. Determination of the oxidation state of redox active enzymes via synchrotron radiation is problematic because exposure to X-rays exerts photoreduction on redox centres. Investigation of artifact-free oxidized enzymes is therefore exceedingly challenging with synchrotron radiation. In the context of class Ib RNRs this affects both the redox active metal centre of R2b and FMN cofactor of NrdI. SFX eliminates the effects of photoreduction observed during synchrotron-based data collection. We describe SFX structures of the R2b-NrdI complex with NrdI in the oxidized and hydroquinone oxidation state. Both 2.0 Å structures are of similar quality as the previously published synchrotron structures of the same complex with a di-iron centre (Hammerstad et al., 2014) showing that the change of methodology does not affect the quality. This allowed detailed examination of structural reorganization induced by changes in FMN redox state. Notably, the FMN conformation *per se* changes little between the oxidized and hydroquinone oxidation state in R2b-NrdI. This is surprising since it was previously shown that FMN is bent in reduced NrdI when not bound to R2b. The complexation of R2b and NrdI thus prevents FMN bending and exerts strain on the isoalloxazine ring in the hydroquinone state. Other flavoproteins have been shown to tune the redox potential of FMN by forcing it into a specific binding angle (Senda et al., 2009; Walsh & Miller, 2003). A recent study by Sorigué et al. presented a SFX

structure of the flavoenzyme fatty acid photodecarboxylase (FAP) in complex with an oxidized flavin cofactor exhibiting a butterfly bending angle of 14° (Sorigué et al., 2021). Using time resolved SFX and complementary approaches, the study showed that during the enzymatic cycle of FAP the conformation of the flavin retains the butterfly bend in the different redox states. The authors conclude that the butterfly bend is enforced by the protein scaffold to promote flavin reduction. Following the same line of reasoning we propose that R2b binding to NrdI restricts FMN bending and thus, opposite to FAP, changes the FMN redox potential of the hydroquinone to favour FMN oxidation and reduction of molecular oxygen to superoxide (Scheme 3). This notion is supported by a study by Cotruvo et al. demonstrating that superoxide production by the *in vitro* R2b-$NrdI_{hq}$ complex of *Bacillus subtilis* is about 40 times faster than the production of superoxide by free $NrdI_{hq}$ under the same experimental conditions (Cotruvo et al., 2013). Controlling the superoxide production by complex formation could serve as a mechanism to protect the cell from production of superoxide by free NrdI. The binding of R2b may also facilitate access of O_2 to FMN by forming a hydrophobic binding pocket around the benzene ring of FMN. O_2 is reduced to superoxide at the C4a atom of the isoalloxazine ring of FMN and we observe a molecule bigger than a water bound about 5 Å away from the C4a atom in the oxidized R2b-NrdI complex. From the experimental setup it seems unlikely that the unidentified molecule is a superoxide ion because FMN never underwent a redox-cycle in this structure. However, refinement with a superoxide ion leaves little residual density, so the binding could fit a molecule of its size (Fig. S3). The density could thus represent a potential binding position of superoxide after its generation (Fig. S3). In addition, the density undergoes a redox-dependent switch of position moving further away from the reactive C4a (7 Å) towards the channel entrance in the reduced R2b-NrdI complex. This move is accompanied by a change of the putative coordination sphere. Importantly, in

422 both oxidized and reduced states, the unknown molecule is integrated into the conserved
423 hydrogen-bonding network connecting FMN and the metal site and switches position with a
424 water. Even though the exact nature of the observed electron density is unknown we
425 conclude that the binding properties of these key positions are controlled by the FMN redox
426 state and could mark the route superoxide would travel after being produced by the FMN.

427 Taken together, our results suggest that the production of superoxide by NrdI and the radical
428 generation in R2b is elegantly orchestrated by the formation of the R2b-NrdI complex as well
429 as redox state control of binding positions (Scheme 3). R2b-NrdI binding induces
430 conformational strain in the flavin, lowering its redox potential and thus promoting
431 superoxide generation. The interaction surface also provides binding positions that are
432 controlled by the redox state of the flavin, presumably involved in gating of channel and metal
433 site access.

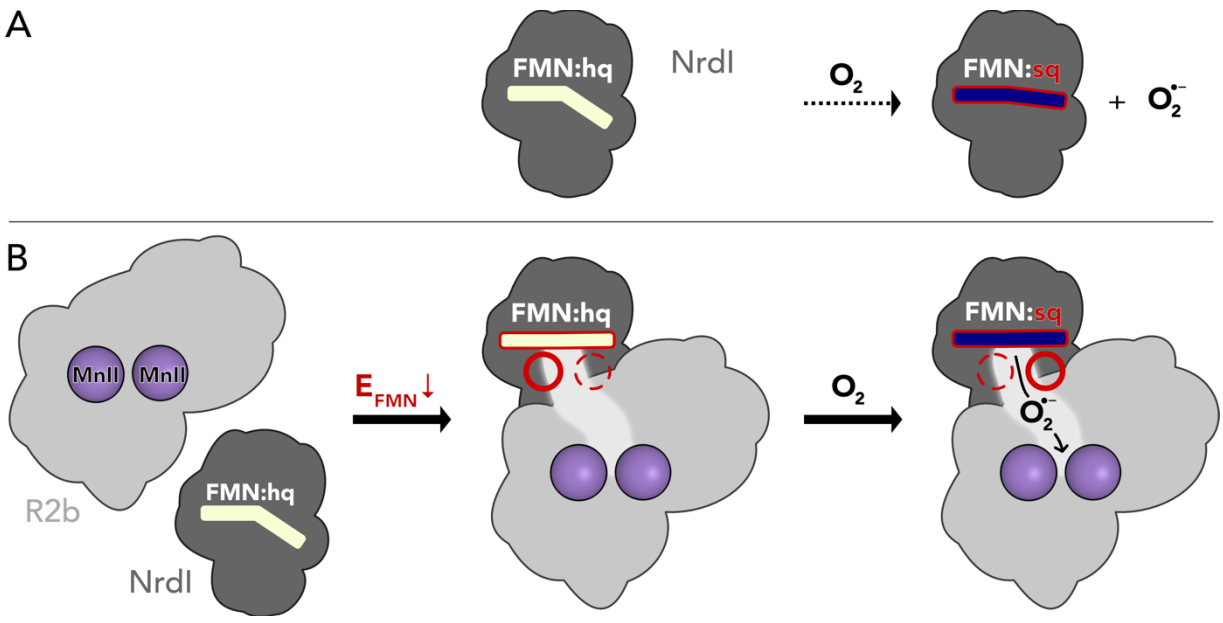

434

435 Scheme 3 **Proposed mechanism for the assembly of the R2b-NrdI complex.** A) Free $NrdI_{hq}$ and molecular oxygen
436 react slowly to produce superoxide and $NrdI_{sq}$. B) R2b and NrdI form a complex which imposes strain on the FMN
437 bend and lowers its redox potential to favour oxygen reduction. The complex formation also generates a redox

state-controlled potential superoxide binding site close to the reactive carbon of FMN. Upon exposure to molecular oxygen, superoxide is generated in the complex and shuttled towards R2b.

Materials and Methods

Protein Expression

The plasmids containing the genes for both *Bc*R2b (pET22b-Bc*r2b*) and *Bc*NrdI (pET22b-Bc*nrdI*) were kindly provided by Marta Hammerstad and Kristoffer Andersson (University of Oslo). The protein expression of *Bc*NrdI was adapted from Røhr et al. (Røhr et al., 2010). *E. coli* BL21(DE3) (New England Biolabs, Frankfurt am Main, Germany) cells were transformed with the pET22b-Bc*nrdI* plasmid. A preculture of Lysogeny Broth medium (Formedium, Norfolk, UK) was inoculated with a single colony, grown over night at 37 °C and 200 rpm. The next day large-scale cultures of 1.6 L Terrific Broth medium (Formedium) per glass bottle supplemented with 100 µg/ml carbenicillin (Alfa Aesar, Kandel, Germany) and 1:10000 v/v antifoam 204 (Merck, Darmstadt, Germany) were inoculated with 0.5% v/v of the preculture. The cells were incubated in a LEX bioreactor (Epiphyte3, Toronto, Canada) at 37 °C until an optical density at 600 nm of about 0.8 was reached. The cultures were cooled down to 20 °C, and the protein expression was induced with 0.8 mM isopropyl β-D-1-thiogalactopyranoside (IPTG) (Formedium). The cells, harvested after 12-16 hours of expression by centrifugation at 4000 g for 20 minutes, formed a dark grey pellet. A volume of 1 L culture formed 12-19 g wet cell pellet. Expression of *Bc*R2b was adapted from Tomter et al. (Tomter et al., 2008) and the protein was expressed in a similar way as *Bc*NrdI. To express *Bc*R2b metal-free, ethylenediaminetetraacetic acid (EDTA) (PanReac AppliChem, Darmstadt, Germany) was added to the large-scale cultures shortly before induction with IPTG to a final concentration of 1 mM. A volume of 1 L culture gave about 8 g wet cell pellet. The pellets were flash-frozen in liquid nitrogen and stored at -20 °C until further use.

Purification

***Bc*NrdI:** The purification of NrdI was adapted from Røhr et al (Røhr et al., 2010). About 20 g of bacterial cell pellet was resuspended in lysis buffer (100 mM Tris-HCl pH 7.5) supplemented with a tablet of EDTA-free cOmplete Protease Inhibitor S2 Cocktail Tablet (PIC) (Roche, Solna, Sweden) and DNase (PanReac Applichem) was added. Cells were lysed with a sonicator, Sonics VCX130 (Sonics, Newtown, CT), and the soluble fraction separated from cell debris by centrifugation at 40000 g for 30 minutes at 4 °C. The NrdI protein was precipitated by slow addition of ammonium sulphate (NH_4SO_4) to the lysate to a final concentration of 60 % w/v (0.37 g/ml) while stirring at 4°C. The precipitate was pelleted by centrifugation at 20000 g for 20 minutes and 4°C and subsequently solubilised with a minimal volume of size exclusion chromatography (SEC) buffer (50 mM Tris pH 7.5). The protein was desalted by dialysis overnight at 4°C against dialysis buffer (10 mM Tris pH 7.5). The desalted protein was filtered through a 0.45 µm filter to remove precipitate and loaded onto a Q Sepharose High Performance 5 ml anion exchange column (Cytiva, Uppsala, Sweden), washed with SEC buffer and eluted with a gradient from 0-50% elution buffer (50 mM Tris-HCl pH 7.5, 1M KCl). The fractions containing the desired protein could be identified by the bright orange colour of NrdI (Fig. S1). Relevant fractions were pooled, concentrated with a Vivaspin 20 centrifugal concentrator with a 30,000 Da molecular weight cut-off polyethersulfone membrane (Vivaspin 30k concentrator) (Sartorius, Göttingen, Germany) and injected onto a HiLoad Superdex 75 prep grade size-exclusion column (Cytiva). Orange fractions were analysed for purity by sodium dodecyl sulphate–polyacrylamide gel electrophoresis (SDS-PAGE) and fractions with a 95% or higher purity were pooled. The theoretical molecular weight of NrdI was calculated to be 13449 Da with ProtParam (Gasteiger et al., 2005) and the extinction

coefficient ε_{447} = 10.8 mM^{-1} cm^{-1} (Berggren et al., 2014) was used to determine the protein concentration using UV-vis spectroscopy. The protein was concentrated to 25 mg/ml, flash frozen in liquid nitrogen and stored at -80 °C until further use.

***Bc*R2b:** The R2b purification protocol was adapted from Tomter et al. (Tomter et al., 2008). The protein was produced metal free; for that purpose, EDTA was included in the lysis buffer to inhibit metal uptake. About 20 g of bacterial cell pellet was resuspended in lysis buffer (100 mM Tris-HCl pH 7.5, 1 mM EDTA) with a tablet of PIC and lysed by sonication. Streptomycin sulphate was added to a total of 2.5% w/v and incubated for 10 minutes at 20° C for DNA precipitation. The crude lysate was cleared by centrifugation for 30 min at 40000 g. The supernatant was cleared from contaminants by adding 40 % (0.24 g/ml) NH_4SO_4 at 20°C followed by centrifugation at 20000 g for 20 minutes. The NH_4SO_4 concentration for the remaining supernatant was increased to 50 % (0.31 g/ml) at 20° to precipitate R2b. After the second centrifugation at 20000g for 20 minutes the pellet was dissolved with a minimal volume of lysis buffer. The protein was diluted 4x with buffer A (50 mM Tris pH 7.5, 1.5 M NH_4SO_4) to increase the salt concentration sufficiently. The diluted protein was filtered through a 0.45 µm membrane filter and loaded onto a column packed with 20 ml Phenyl Sepharose High Performance resin (Cytiva). The protein was washed with buffer A and eluted with a gradient with SEC buffer (50 mM Tris pH 7.5). Several column volumes were needed to elute the protein. The elution fractions were analysed by SDS-PAGE. Protein containing fractions were pooled, concentrated by a Vivaspin 50k concentrator and injected onto a HiLoad Superdex 200 prep grade column (Cytiva). Elution fractions were analysed by SDS-PAGE and pure fractions pooled. The theoretical molecular weight and the extinction co-efficient of R2b were calculated with ProtParam to be 37017 Da and ε_{280} = 48.36 mM^{-1} cm^{-1}

511 respectively (Gasteiger et al., 2005). R2b was concentrated to 50 mg/ml with a Vivaspin 50kDa
512 concentrator, flash frozen and stored at -80 °C until further use. A total of 20 g bacterial cell
513 pellet yielded about 100-150 mg pure protein.
514

515 ## Quantification of R2b metal content with TXRF

516 To control the metal content of *Bc*R2b the protein was measured with total reflection x-ray
517 fluorescence spectroscopy (TXRF) using a Bruker PicoFox S2 spectrometer (Bruker, Billerica,
518 MA). Three independently prepared replicates of the concentrated protein at 1.7 mM were
519 mixed 1:1 with a gallium standard at 20 mg/l and dried on top of a siliconized quartz sample
520 carrier. The discs were individually measured before use to avoid external contamination of
521 the sample. The results were analysed with the Bruker Spectra software version 7.8.2.0
522 provided with the instrument.
523

524 ## Crystallization of the *Bc*R2b-NrdI complex

525 The *Bc*R2b-NrdI protein complex was prepared for crystallization as follows: 0.25 mM *Bc*R2b
526 in 50 mM Tris-HCl pH 7.5 was incubated with 12 molar equivalents of $MnCl_2$ for 10 minutes
527 at 20° C, then 0.25 mM *Bc*NrdI was added and the mixture incubated for another 15 minutes
528 at 20° C to ensure complex formation. New crystallization conditions were screened since the
529 crystallization condition published in (Hammerstad et al., 2014) could not be reproduced.
530 Initial hits in conditions C5 of the JSCG+ crystallisation screen (0.1 M Sodium Hepes pH 7.5,
531 0.8 M Sodium phosphate monobasic monohydrate,0.8 M Potassium phosphate monobasic)
532 and the A7 condition of the PACT premier crystallization screen (0.1 M Sodium acetate pH
533 5.0, 0.2 M NaCl, 20 % w/v PEG 6000) (both Molecular Dimensions, Sheffield, UK) were further
534 optimized to yield crystals between 10 µm and 50 µm in the longest axis (Fig. S1). The final

crystallization protocol was established as described: Crystals spontaneously grew in a hanging drop vapour diffusion experiment after one to two days at 20°C. Crystallization condition A (0.1 M Hepes pH 7.0, 0.6-0.85 M sodium phosphate monobasic monohydrate, 0.6-0.85 M potassium phosphate monobasic) was manually mixed with the protein complex solution in a ratio of 1:1 (1 µl + 1 µl). The crystals grown in this experiment were used to produce microseeds for crystallization with the batch method. Two crystal containing drops were transferred into 50 µl of crystallization condition A in the bottom of a 1.5 ml microcentrifuge tube. A seed bead (Saint Gobain, Aachen, Germany) was placed into the solution, the crystal crushed by vigorous shaking and the mixture used as seed stock for the following crystallization experiments. Batch crystallization was set up in PCR tubes at 20 °C. A volume of 40 µl of crystallization condition B (0.1 M $MnCl_2$, 0.1 M sodium acetate 5.0, 5% PEG 6000) were pipetted on top of 40 µl of protein complex solution. A volume of 8 µl of microseed solution was added to the tube and everything mixed by pipetting. Orange rhombohedron shaped crystals typically sized between 20 and 50 µm in the longest axis grew over night, forming an orange pellet at the bottom of the tubes. The crystals were resuspended and pooled in 2 ml microcentrifuge tubes (Fig. S1). Crystals used to collect the dataset for *Bc*R2b$_{MnMn}$-NrdI$_{ox}$ could be directly loaded into a Gastight SampleLock (Hamilton, Bonaduz, Switzerland) syringe for sample delivery. The crystals used for the *Bc*R2b$_{MnMn}$-NrdI$_{hq}$ dataset had to be chemically reduced first as described below.

Reduction protocol

Crystals for the *Bc*R2b$_{MnMn}$-NrdI$_{hq}$ dataset were chemically reduced before data collection. All following steps were conducted in an anaerobic glove box with O_2 below 10 ppm at room temperature. A volume of 900 µl of pooled crystal slurry was gently centrifuged, forming a

dense crystal pellet. Of the supernatant 800 µl were carefully removed, collected separately and supplemented with 18 µl of freshly prepared, anaerobic 1 M sodium dithionite (DT). The DT-containing supernatant was gently mixed with the crystal pellet (final DT concentration of 20 mM) and the colour change of the crystals from a bright orange to a faint, light yellow was observed in a matter of minutes. The DT was subsequently washed out by gently spinning down the crystals, removing the supernatant without disturbing the crystal pellet, replacing it with anaerobic wash buffer (100 mM $MnCl_2$, 50 mM sodium acetate pH 5.0, 2.5% (w/v) PEG 6000, 10% (v/v) glycerol) and gently resuspending the crystals. This washing step was repeated 3 times, adding wash buffer in the last step to a volume of 800 µl. The final concentration of DT in the crystal slurry was below 4 µM. All of the crystal slurry was loaded into a 1 ml gastight SampleLock Hamilton syringe and stored in the anaerobic box until sample injection.

Data collection

The *Bc*R2b-NrdI crystals were initially tested for stability and diffraction quality at SACLA in Japan during experiment 2017B8085. The sample was delivered with a grease extruder setup installed on site (Sugahara et al., 2015; Tono et al., 2013). Hydroxyethyl cellulose matrix (Sugahara et al., 2017) and the protein crystals were mixed together in a volume ratio matrix to crystal pellet of 9:1 and the mixture ejected with a HPLC pump through a 150 µm nozzle with a flow rate of 1-1.5 µl/min, delivering the sample into the XFEL beam. X-rays were delivered as <10 fs long pulses at 10.9 keV with 30 Hz repetition rate and a typical pulse energy of around 0.32 mJ with a beam size of 2 x 2 μm^2 (fwhm). The diffraction of the sample was recorded 100 mm downstream of the interaction point on an Octal MPCCD detector. The

initial data collection showed stability of the crystals over days and a diffraction quality to about 2 Å.

The datasets used in this paper were collected at LCLS, California during experiment LU50. X-ray pulses at 9.5 keV with a pulse energy of 4 mJ, 30 Hz repetition rate and a duration of around 35 fs were generated and used for X-ray diffraction in the macromolecular femtosecond crystallography (MFX) experimental hutch (Sierra et al., 2019); the diffraction was recorded on a Rayonix MX340 (Rayonix L.L.C, Evanston, USA) detector. The sample was delivered into the X-ray interaction point with the drop-on-tape method; the detailed method was described by Fuller et. al (Fuller et al., 2017). Briefly, crystal slurry in a 1 ml SampleLock syringe was pumped with a syringe pump (KD scientific, Holliston, MA) at a flow rate of 8-9 µl/min through a silica capillary into a 6 µl sample reservoir. An acoustic transducer transferred crystal containing droplets of 2.5-4 nl volume onto a Kapton tape, which transported the droplets into the X-ray beam at 28° C and 27% relative humidity with a speed of 300 mm/s, which resulted in the crystals being exposed to the He-environment for about 0.8 s. The enclosure of the setup was filled with a He-atmosphere with an O_2 level below 0.1 % for the *Bc*R2b$_{MnMn}$-NrdI$_{hq}$ data collection.

Processing, Structure Determination and Refinement

The datasets for *Bc*R2b$_{MnMn}$-NrdI$_{hq}$ and *Bc*R2b$_{MnMn}$-NrdI$_{ox}$ were processed with cctbx.xfel (Brewster, Young, et al., 2019; Hattne et al., 2014; Sauter, 2015) and DIALS (Brewster et al., 2018; Winter et al., 2018). We performed joint refinement of the crystal models against the detector position for each batch to account for small time-dependent variations in detector position and also corrected for the Kapton tape shadow (Fuller et al., 2017). Data was scaled and merged to 2.0 Å resolution using cctbx.xfel.merge with errors determined by the ev11

606 method (Brewster, Bhowmick, et al., 2019) based on $CC_{1/2}$ and multiplicity values and on R-
607 factors after initial refinement. Data statistics are available in Table 1. Both structures were
608 solved by molecular replacement and refined independently with the PHENIX Suite
609 (Liebschner et al., 2019). The phases were solved with phenix.phaser (McCoy et al., 2007). A
610 *Bc*R2b-NrdI complex structure (PDB ID: 4BMO (Hammerstad et al., 2014)) was modified by
611 manually removing waters and alternate conformations and used as a starting model. The
612 suggested solutions were in the same space group ($C222_1$) as the starting model with similar
613 unit cell dimensions (Table 1) with one complex in the asymmetric unit. The R_{free} set of the
614 4BMO model corresponding to 5% of reflections was assigned to all datasets with
615 phenix.reflection_tools. Restraints of the entry "FMN" of the ligand database provided by
616 phenix were used for the oxidized FMN in *Bc*R2b$_{MnMn}$-NrdI$_{ox}$. Restraints for the hydroquinone
617 FMN in *Bc*R2b$_{MnMn}$-NrdI$_{hq}$ were generated with phenix eLBOW (Moriarty et al., 2009). The
618 datasets were iteratively refined with phenix.refine (Afonine et al., 2012), examined and built
619 in coot (Emsley et al., 2010) and validated with MolProbity (Williams et al., 2018). Refinement
620 of all atoms included isotropic B-factors, TLS parameters, occupancy and reciprocal space
621 refinement with a high-resolution cut off of 2.0 Å. Waters were initially added using
622 phenix.refine and in later refinements corrected manually. The metal occupancy for the
623 reduced structure was fixed manually after several cycles of refinement. An overview over
624 refinement and model quality statistics can be found in Table 1, created with
625 phenix.table_one. The refined structures were compared and RMSD values calculated with
626 SSM superimpose (Krissinel & Henrick, 2004).

627 ## Figures

628 Molecular figures were prepared with the PyMOL Molecular Graphics System, Version 2.4.2
629 Schrödinger, LLC. Scheme 2 was designed with ChemDraw (PerkinElmer Informatics). The bar

graph in Fig. 3 A was generated with GraphPad Prism, Version 9.2.0 for iOS (GraphPad Software, San Diego, California USA). All figures and schemes except Scheme 2 were designed and assembled in Affinity Designer (Serif (Europe) Ltd, Nottingham, UK)

Acknowledgements

We thank Robert Bolotovsky, Iris D. Young and Lee J. O'Riordan for help with data processing and the staff at LCLS and SACLA. We thank Kristine Grāve for input and helpful discussions during data analysis and manuscript writing.

This work was supported by the Swedish Research Council (2017-04018 and 2021-03992 to M.H.), the European Research Council (HIGH-GEAR 724394 to M.H.), the Knut and Alice Wallenberg Foundation (20217.0275 and 2019.0436 to M.H.), and National Institutes of Health grants GM133081 (to K.D.S.), GM117126 (to N.K.S.), GM55302 (to V.K.Y.), GM110501 (to J.Y.) and GM126289 (to J.K.). A.M.O., P.A., and A.Bu. were supported by Diamond Light Source, the UK Science and Technology Facilities Council (STFC), a jointly funded strategic award from the Wellcome Trust and the Biotechnology and Biological Sciences Research Council (102593 to James Naismith), a Wellcome Investigator Award (210734/Z/18/Z to A.M.O.), and a Royal Society Wolfson Fellowship (RSWF\R2\182017 to A.M.O.). The DOT instrument used in this research was funded by Department of Energy (DOE), Office of Science, Office of Basic Energy Sciences (BES), Division of Chemical Sciences, Geosciences, and Biosciences (to J.K., J.Y., and V.K.Y.). XFEL data was collected under proposal LU50 at LCLS, SLAC, Stanford, USA, and under proposal 2017B8085 at BL2 of SACLA, Japan. The Rayonix detector used at LCLS was supported by the NIH grant S10 OD023453. Use of the LCLS, SLAC National Accelerator Laboratory, is supported by the U.S. DOE, Office of Science, BES, under contract no. DE-AC02-76SF00515.

Author Contributions

J.J., H.L., V.S., O.A. and M.H. developed the study

C.P., I-S.K., S.G., P.S.S., A.M.O., F.D.F., and J.K. developed, tested and ran the sample delivery system

A.S.B., M.D., K.D.S., A.Bh., A.Bu., and N.K.S. processed and analysed XFEL data

F.D.F., A.Ba. operated the MFX instrument

J.J., H.L., O.A., M.H., C.P., I-S.K., A.S.B., S.G., K.D.S., A.Bh., P.S.S., A.Bu., P.A., A.M.O., F.D.F., A.Ba., N.K.S., V.K.Y., J.Y., J.K. performed the LCLS experiment

V.S., H.L., P.A., F.D.F., M.H., M.H.C., A.M.O., S.O., K.T., V.K.Y., J.K., J.Y. performed the SACLA experiment

J.J. and H.L. produced and purified proteins and developed the crystallization protocol

J.J. refined, analysed and interpreted the data and wrote the manuscript with input from all authors

H.L. and M.H. supervised, edited and revised the manuscript

Competing interests

The authors declare no competing interests.

Data availability

The atomic coordinates and crystallographic data have been deposited in the Protein Data Bank (https ://www.pdb.org/) under the following accession codes: *Bc*R2b$_{MnMn}$-NrdI$_{ox}$: 7Z3D; *Bc*R2b$_{MnMn}$-NrdI$_{hq}$: 7Z3E.

References:

Afonine, P. V., Grosse-Kunstleve, R. W., Echols, N., Headd, J. J., Moriarty, N. W., Mustyakimov, M., Terwilliger, T. C., Urzhumtsev, A., Zwart, P. H., & Adams, P. D. (2012). Towards automated crystallographic structure refinement with phenix.refine. *Acta Crystallographica Section D: Biological Crystallography*, *68*(4), 352–367. https://doi.org/10.1107/S0907444912001308

Berggren, G., Duraffourg, N., Sahlin, M., & Sjöberg, B. M. (2014). Semiquinone-induced maturation of bacillus anthracis ribonucleotide reductase by a superoxide intermediate. *Journal of Biological Chemistry*, *289*(46), P31940-31949. https://doi.org/10.1074/jbc.M114.592535

Blaesi, E. J., Palowitch, G. M., Hu, K., Kim, A. J., Rose, H. R., Alapati, R., Lougee, M. G., Kim, H. J., Taguchi, A. T., Tan, K. O., Laremore, T. N., Griffin, R. G., Krebs, C., Matthews, M. L., Silakov, A., Bollinger, J. M., Allen, B. D., & Boal, A. K. (2018). Metal-free class Ie ribonucleotide reductase from pathogens initiates catalysis with a tyrosinederived dihydroxyphenylalanine radical. *Proceedings of the National Academy of Sciences of the United States of America*, *115*(40), 10022–10027. https://doi.org/10.1073/pnas.1811993115

Boal, A. K., Cotruvo, J. A., Stubbe, J. A., & Rosenzweig, A. C. (2010). Structural basis for activation of class Ib ribonucleotide reductase. *Science*, *329*(5998), 1526–1530. https://doi.org/10.1126/science.1190187

Brewster, A. S., Bhowmick, A., Bolotovsky, R., Mendez, D., Zwarta, P. H., & Sauter, N. K. (2019). SAD phasing of XFEL data depends critically on the error model. *Urn:Issn:2059-7983*, *75*(11), 959–968. https://doi.org/10.1107/S2059798319012877

Brewster, A. S., Waterman, D. G., Parkhurst, J. M., Gildea, R. J., Young, I. D., O'Riordan, L. J., Yano, J., Winter, G., Evans, G., & Sauter, N. K. (2018). Improving signal strength in serial crystallography with DIALS geometry refinement. *Acta Crystallographica. Section D, Structural Biology*, *74*(Pt 9), 877–894. https://doi.org/10.1107/S2059798318009191

Brewster, A. S., Young, I. D., Lyubimov, A., Bhowmick, A., & Sauter, N. K. (2019). Processing serial crystallographic data from XFELs or synchrotrons using the cctbx.xfel GUI. *Computational Crystallography Newsletter*, *10*, 22–39.

Carugo, O. (2014). Buried chloride stereochemistry in the protein data bank. *BMC Structural Biology*, *14*(1), 1–7. https://doi.org/10.1186/s12900-014-0019-8

Cotruvo, J. A., Stich, T. A., Britt, R. D., & Stubbe, J. (2013). Mechanism of assembly of the dimanganese-tyrosyl radical cofactor of class Ib ribonucleotide reductase: Enzymatic generation of superoxide is required for tyrosine oxidation via a Mn(III)Mn(IV) intermediate. *Journal of the American Chemical Society*, *135*(10), 4027–4039. https://doi.org/10.1021/ja312457t

Cotruvo, J. A., & Stubbe, J. (2008). NrdI, a flavodoxin involved in maintenance of the diferric-tyrosyl radical cofactor in Escherichia coli class Ib ribonucleotide reductase. *Proceedings of the National Academy of Sciences of the United States of America*, *105*(38), 14383–14388. https://doi.org/10.1073/pnas.0807348105

Cotruvo, J. A., & Stubbe, J. (2010). An active dimanganese(III)-tyrosyl radical cofactor in escherichia coli class Ib ribonucleotide reductase. *Biochemistry*, *49*(6), 1297–1309. https://doi.org/10.1021/bi902106n

Cox, N., Ogata, H., Stolle, P., Reijerse, E., Auling, G., & Lubitz, W. (2010). A Tyrosyl-Dimanganese Coupled Spin System is the Native Metalloradical Cofactor of the R2F Subunit of the Ribonucleotide Reductase of Corynebacterium ammoniagenes. *Journal of the American Chemical Society*, *132*(32), 11197–11213. https://doi.org/10.1021/ja1036995

Doerr, A. (2011). Diffraction before destruction. In *Nature Methods* (Vol. 8, Issue 4, p. 283). https://doi.org/10.1038/nmeth0411-283

Emsley, P., Lohkamp, B., Scott, W. G., & Cowtan, K. (2010). Features and development of Coot. *Acta Crystallographica. Section D, Biological Crystallography*, *66*(Pt 4), 486–501. https://doi.org/10.1107/S0907444910007493

Fuller, F. D., Gul, S., Chatterjee, R., Burgie, E. S., Young, I. D., Lebrette, H., Srinivas, V., Brewster, A. S., Michels-Clark, T., Clinger, J. A., Andi, B., Ibrahim, M., Pastor, E., de Lichtenberg, C., Hussein, R., Pollock, C. J., Zhang, M., Stan, C. A., Kroll, T., … Yano, J. (2017). Drop-on-demand sample delivery for studying biocatalysts in action at X-ray free-electron lasers. *Nature Methods*, *14*(4), 443–449. https://doi.org/10.1038/nmeth.4195

Gasteiger, E., Hoogland, C., Gattiker, A., Duvaud, S., Wilkins, M. R., Appel, R. D., & Bairoch, A. (2005). Protein Identification and Analysis Tools on the ExPASy Server. In *The Proteomics Protocols Handbook* (pp. 571–607). Humana Press. https://doi.org/10.1385/1-59259-890-0:571

Ghisla, S., & Massey, V. (1989). Mechanisms of flavoprotein-catalyzed reactions. *European Journal of*

Biochemistry, *181*(1), 1–17. https://doi.org/10.1111/J.1432-1033.1989.TB14688.X

Grāve, K., Lambert, W., Berggren, G., Griese, J. J., Bennett, M. D., Logan, D. T., & Högbom, M. (2019). Redox-induced structural changes in the di-iron and di-manganese forms of Bacillus anthracis ribonucleotide reductase subunit NrdF suggest a mechanism for gating of radical access. *Journal of Biological Inorganic Chemistry*, *24*(6), 849–861. https://doi.org/10.1007/s00775-019-01703-z

Hammerstad, M., Hersleth, H. P., Tomter, A. B., Røhr, Å. K., & Andersson, K. K. (2014). Crystal structure of Bacillus cereus class Ib ribonucleotide reductase di-iron NrdF in complex with NrdI. *ACS Chemical Biology*, *9*(2), 526–537. https://doi.org/10.1021/cb400757h

Hattne, J., Echols, N., Tran, R., Kern, J., Gildea, R. J., Brewster, A. S., Alonso-Mori, R., Glöckner, C., Hellmich, J., Laksmono, H., Sierra, R. G., Lassalle-Kaiser, B., Lampe, A., Han, G., Gul, S., DiFiore, D., Milathianaki, D., Fry, A. R., Miahnahri, A., … Sauter, N. K. (2014). Accurate macromolecular structures using minimal measurements from X-ray free-electron lasers. *Nature Methods 2014 11:5*, *11*(5), 545–548. https://doi.org/10.1038/nmeth.2887

Högbom, M., Sjöberg, B., & Berggren, G. (2020). Radical Enzymes. In *eLS* (Vol. 1, pp. 375–393). Wiley. https://doi.org/10.1002/9780470015902.a0029205

Huque, Y., Fieschi, F., Torrents, E., Gibert, I., Eliasson, R., Reichard, P., Sahlin, M., & Sjoberg, B. M. (2000). The active form of the R2F protein of class Ib ribonucleotide reductase from Corynebacterium ammoniagenes is a diferric protein. *Journal of Biological Chemistry*, *275*(33), 25365–25371. https://doi.org/10.1074/jbc.M002751200

Johansson, R., Torrents, E., Lundin, D., Sprenger, J., Sahlin, M., Sjöberg, B. M., & Logan, D. T. (2010). High-resolution crystal structures of the flavoprotein NrdI in oxidized and reduced states - An unusual flavodoxin: Structural biology. *FEBS Journal*, *277*(20), 4265–4277. https://doi.org/10.1111/j.1742-4658.2010.07815.x

Krissinel, E., & Henrick, K. (2004). Secondary-structure matching (SSM), a new tool for fast protein structure alignment in three dimensions. *Acta Crystallographica. Section D, Biological Crystallography*, *60*(Pt 12 Pt 1), 2256–2268. https://doi.org/10.1107/S0907444904026460

Liebschner, D., Afonine, P. V., Baker, M. L., Bunkoczi, G., Chen, V. B., Croll, T. I., Hintze, B., Hung, L. W., Jain, S., McCoy, A. J., Moriarty, N. W., Oeffner, R. D., Poon, B. K., Prisant, M. G., Read, R. J., Richardson, J. S., Richardson, D. C., Sammito, M. D., Sobolev, O. V., … Adams, P. D. (2019). Macromolecular structure determination using X-rays, neutrons and electrons: Recent developments in Phenix. *Acta Crystallographica Section D: Structural Biology*, *75*(10), 861–877. https://doi.org/10.1107/S2059798319011471

Makhlynets, O., Boal, A. K., Rhodes, D. L. V., Kitten, T., Rosenzweig, A. C., & Stubbe, J. A. (2014). Streptococcus sanguinis class Ib ribonucleotide reductase: High activity with both iron and manganese cofactors and structural insights. *Journal of Biological Chemistry*, *289*(9), 6259–6272. https://doi.org/10.1074/jbc.M113.533554

McCoy, A. J., Grosse-Kunstleve, R. W., Adams, P. D., Winn, M. D., Storoni, L. C., & Read, R. J. (2007). Phaser crystallographic software. *Journal of Applied Crystallography*, *40*(4), 658–674. https://doi.org/10.1107/S0021889807021206

Moriarty, N. W., Grosse-Kunstleve, R. W., & Adams, P. D. (2009). electronic Ligand Builder and Optimization Workbench (eLBOW): a tool for ligand coordinate and restraint generation. *Urn:Issn:0907-4449*, *65*(10), 1074–1080. https://doi.org/10.1107/S0907444909029436

Nass, K. (2019). Radiation damage in protein crystallography at X-ray free-electron lasers. *Urn:Issn:2059-7983*, *75*(2), 211–218. https://doi.org/10.1107/S2059798319000317

Neutze, R., Wouts, R., Van Der Spoel, D., Weckert, E., & Hajdu, J. (2000). Potential for biomolecular imaging with femtosecond X-ray pulses. *Nature*, *406*(6797), 752–757. https://doi.org/10.1038/35021099

Nordlund, P., & Reichard, P. (2006). Ribonucleotide reductases. *Annual Review of Biochemistry*, *75*(1), 681–706. https://doi.org/10.1146/ annurev.biochem.75.103004.142443

Roca, I., Torrents, E., Sahlin, M., Gibert, I., & Sjöberg, B.-M. M. (2008). NrdI Essentiality for Class Ib Ribonucleotide Reduction in Streptococcus pyogenes. *Journal of Bacteriology*, *190*(14), 4849–4858. https://doi.org/10.1128/JB.00185-08

Røhr, Å. K., Hersleth, H.-P. P., Kristoffer Andersson, K., & Andersson, K. K. (2010). Tracking flavin conformations in protein crystal structures with raman spectroscopy and QM/MM calculations. *Angewandte Chemie - International Edition*, *49*(13), 2324–2327. https://doi.org/10.1002/anie.200907143

Rould, M. A., & Carter, C. W. (2003). Isomorphous Difference Methods. *Methods in Enzymology*, *374*, 145–163. https://doi.org/10.1016/S0076-6879(03)74007-5

Sauter, N. K. (2015). XFEL diffraction: developing processing methods to optimize data quality. *Journal of*

Synchrotron Radiation, *22*(2), 239–248. https://doi.org/10.1107/S1600577514028203

Senda, T., Senda, M., Kimura, S., & Ishida, T. (2009). Redox control of protein conformation in flavoproteins. In *Antioxidants and Redox Signaling* (Vol. 11, Issue 7, pp. 1741–1766). Antioxid Redox Signal. https://doi.org/10.1089/ars.2008.2348

Sierra, R. G., Batyuk, A., Sun, Z., Aquila, A., Hunter, M. S., Lane, T. J., Liang, M., Yoon, C. H., Alonso-Mori, R., Armenta, R., Castagna, J.-C., Hollenbeck, M., Osier, T. O., Hayes, M., Aldrich, J., Curtis, R., Koglin, J. E., Rendahl, T., Rodriguez, E., … IUCr. (2019). The Macromolecular Femtosecond Crystallography Instrument at the Linac Coherent Light Source. *Urn:Issn:1600-5775*, *26*(2), 346–357. https://doi.org/10.1107/S1600577519001577

Sorigué, D., Hadjidemetriou, K., Blangy, S., Gotthard, G., Bonvalet, A., Coquelle, N., Samire, P., Aleksandrov, A., Antonucci, L., Benachir, A., Boutet, S., Byrdin, M., Cammarata, M., Carbajo, S., Cuiné, S., Doak, R. B., Foucar, L., Gorel, A., Grünbein, M., … Beisson, F. (2021). Mechanism and dynamics of fatty acid photodecarboxylase. *Science*, *372*(6538). https://doi.org/10.1126/science.abd5687

Spence, J. C. H. (2017). XFELs for structure and dynamics in biology. *IUCrJ*, *4*(Pt 4), 322. https://doi.org/10.1107/S2052252517005760

Srinivas, V., Lebrette, H., Lundin, D., Kutin, Y., Sahlin, M., Lerche, M., Eirich, J., Branca, R. M. M., Cox, N., Sjöberg, B. M., & Högbom, M. (2018). Metal-free ribonucleotide reduction powered by a DOPA radical in Mycoplasma pathogens. *Nature*, *563*(7731), 416–420. https://doi.org/10.1038/s41586-018-0653-6

Sugahara, M., Mizohata, E., Nango, E., Suzuki, M., Tanaka, T., Masuda, T., Tanaka, R., Shimamura, T., Tanaka, Y., Suno, C., Ihara, K., Pan, D., Kakinouchi, K., Sugiyama, S., Murata, M., Inoue, T., Tono, K., Song, C., Park, J., … Iwata, S. (2015). Grease matrix as a versatile carrier of proteins for serial crystallography. *Nature Methods*, *12*(1), 61–63. https://doi.org/10.1038/nmeth.3172

Sugahara, M., Nakane, T., Masuda, T., Suzuki, M., Inoue, S., Song, C., Tanaka, R., Nakatsu, T., Mizohata, E., Yumoto, F., Tono, K., Joti, Y., Kameshima, T., Hatsui, T., Yabashi, M., Nureki, O., Numata, K., Nango, E., & Iwata, S. (2017). Hydroxyethyl cellulose matrix applied to serial crystallography. *Scientific Reports 2017 7:1*, *7*(1), 1–9. https://doi.org/10.1038/s41598-017-00761-0

Tomter, A. B., Bell, C. B., Røhr, A. K., Andersson, K. K., Solomon, E. I., Røhr, Å. K., Andersson, K. K., & Solomon, E. I. (2008). Circular dichroism and magnetic circular dichroism studies of the biferrous site of the class Ib ribonucleotide reductase from Bacillus cereus: comparison to the class Ia enzymes. *Biochemistry*, *47*(43), 11300–11309. https://doi.org/10.1021/bi801212f

Tono, K., Togashi, T., Inubushi, Y., Sato, T., Katayama, T., Ogawa, K., Ohashi, H., Kimura, H., Takahashi, S., Takeshita, K., Tomizawa, H., Goto, S., Ishikawa, T., & Yabashi, M. (2013). Beamline, experimental stations and photon beam diagnostics for the hard x-ray free electron laser of SACLA. *New Journal of Physics*, *15*(8), 083035. https://doi.org/10.1088/1367-2630/15/8/083035

Walsh, J. D., & Miller, A. F. (2003). Flavin reduction potential tuning by substitution and bending. *Journal of Molecular Structure: THEOCHEM*, *623*(1–3), 185–195. https://doi.org/10.1016/S0166-1280(02)00719-4

Williams, C. J., Headd, J. J., Moriarty, N. W., Prisant, M. G., Videau, L. L., Deis, L. N., Verma, V., Keedy, D. A., Hintze, B. J., Chen, V. B., Jain, S., Lewis, S. M., Arendall, W. B., Snoeyink, J., Adams, P. D., Lovell, S. C., Richardson, J. S., & Richardson, D. C. (2018). MolProbity: More and better reference data for improved all-atom structure validation. *Protein Science*, *27*(1), 293–315. https://doi.org/10.1002/pro.3330

Winter, G., Waterman, D. G., Parkhurst, J. M., Brewster, A. S., Gildea, R. J., Gerstel, M., Fuentes-Montero, L., Vollmar, M., Michels-Clark, T., Young, I. D., Sauter, N. K., Evans, G., & IUCr. (2018). DIALS: implementation and evaluation of a new integration package. *Urn:Issn:2059-7983*, *74*(2), 85–97. https://doi.org/10.1107/S2059798317017235

Zheng, Y. J., & Ornstein, R. L. (1996). A Theoretical Study of the Structures of Flavin in Different Oxidation and Protonation States. *Journal of the American Chemical Society*, *118*(39), 9402–9408. https://doi.org/10.1021/JA9608151

Supplementary Information

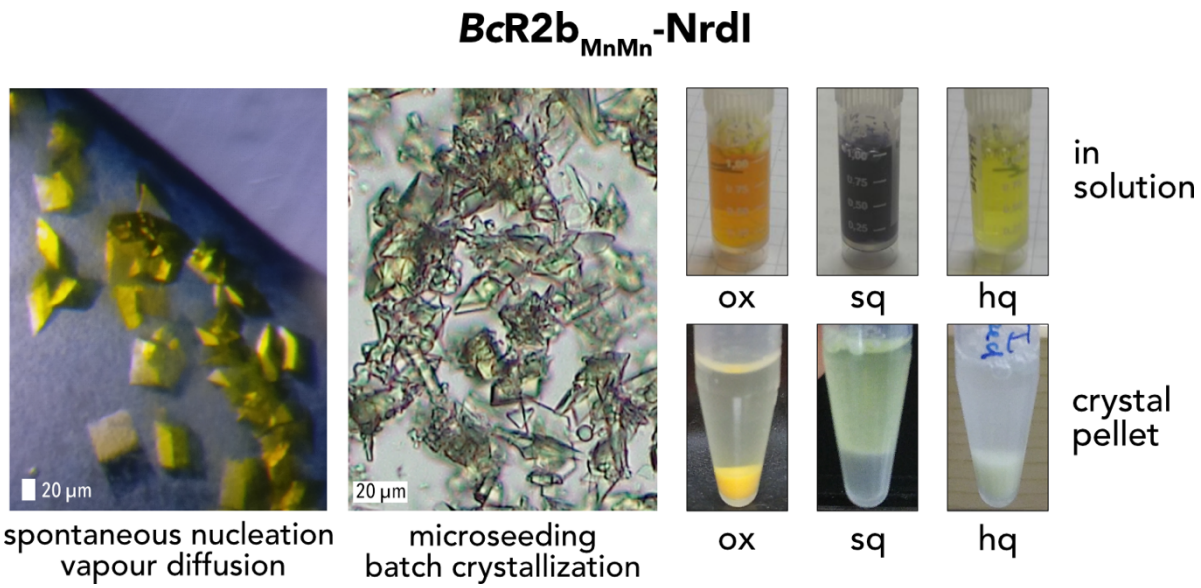

S 1 **Crystallization of the di-manganese *Bc*R2b-NrdI complex**. Spontaneous nucleation yields crystals of the length of 100 µm or longer. In the batch crystallization, crystals are significantly smaller with most crystals between 20 and 50 µm. For the two pictures on the left side, crystals of the complex with NrdI in the oxidized state are viewed under an optical microscope. On the right side, pictures are shown for the complex in solution (top row) and in crystals (bottom row) with NrdI in the oxidized, semiquinone and hydroquinone states. The oxidation state of FMN changes the colour of the complex in both solution and crystals.

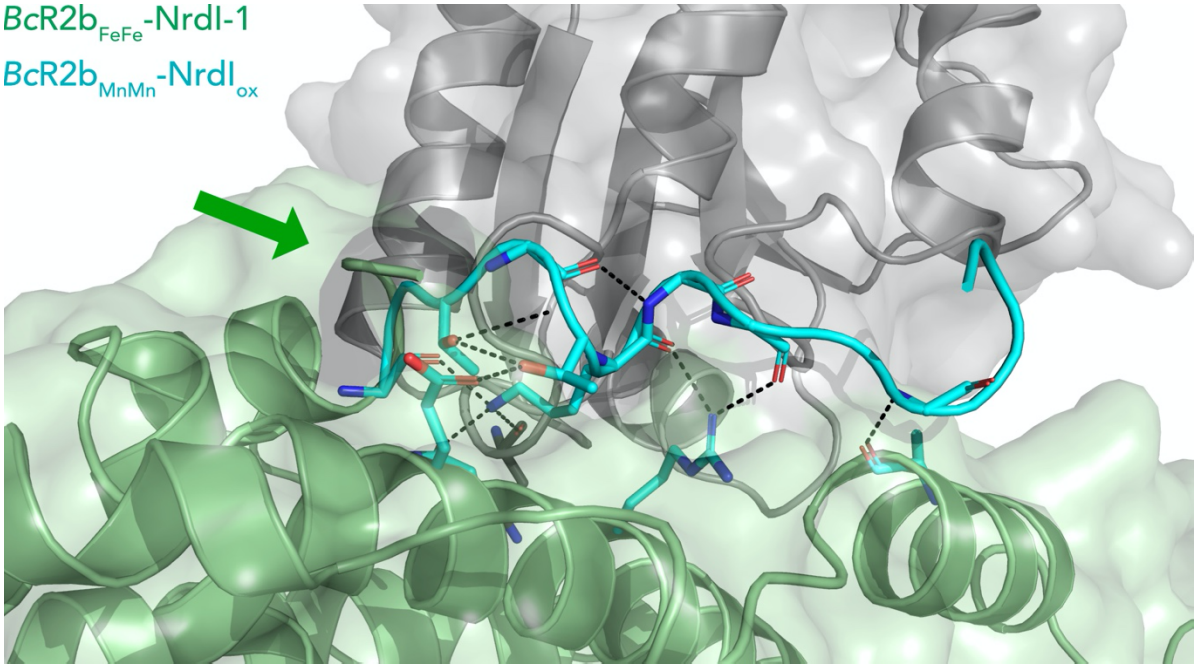

S 2 **Extended C-terminus in *Bc*R2b$_{MnMn}$-NrdI$_{ox}$.** Superposition of *Bc*R2b$_{FeFe}$-NrdI-1 (PDB ID: 4BMO) (pale green for R2b and grey for NrdI) and *Bc*R2b$_{MnMn}$-NrdI$_{ox}$ (in cyan) showing an extension of the ordered C-terminus by 9 amino acids. The green arrow points towards the C-terminus of *Bc*R2b$_{FeFe}$-NrdI-1. The C-terminus is situated in a groove between R2b and NrdI; hydrogen bonds are shown with black dashed lines and bonded side chains are shown as sticks.

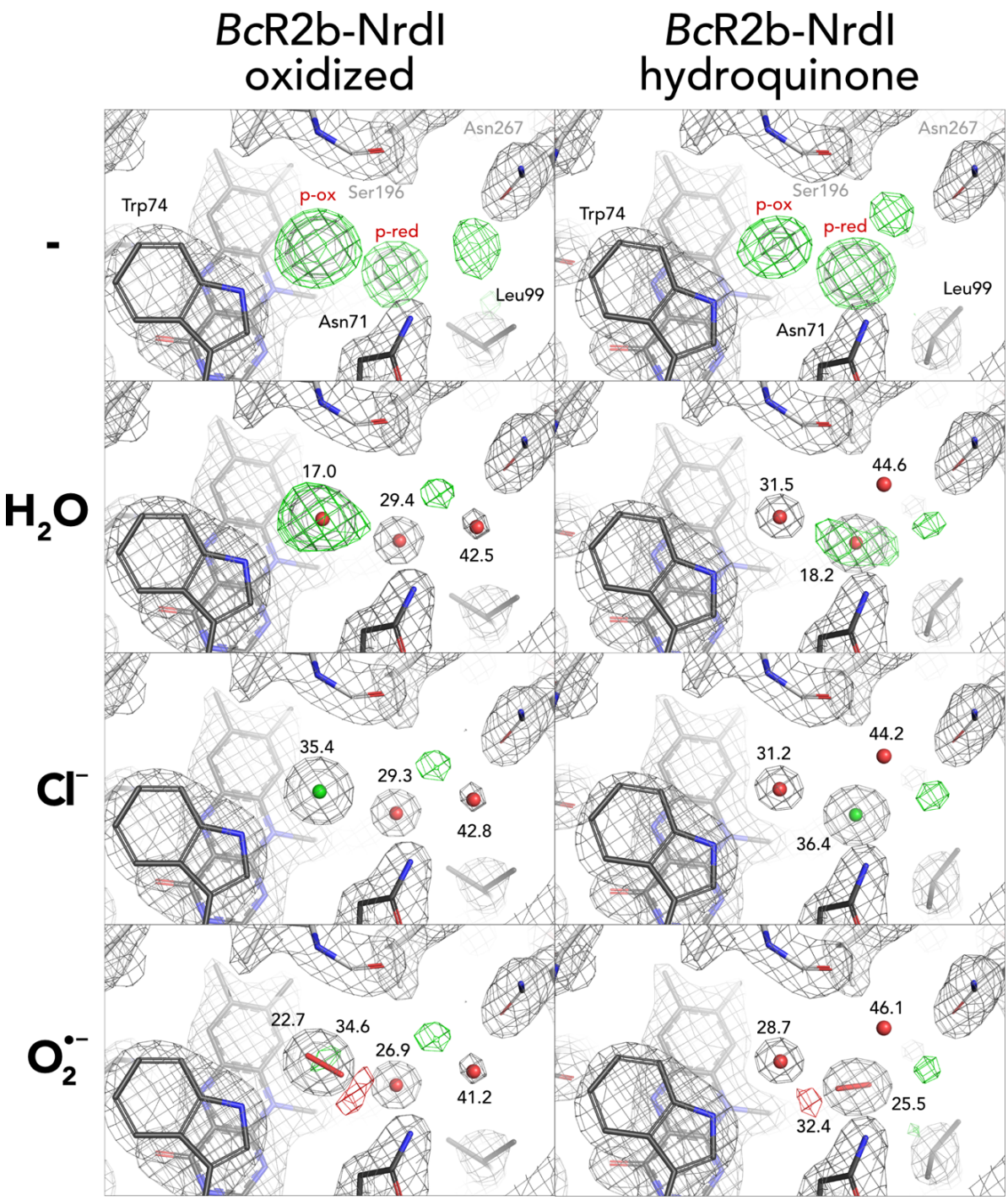

S 3 **Different modelling results for unidentified density close to FMN**. Results for both oxidized and hydroquinone *Bc*R2b-NrdI complex structures. 2Fo-Fc maps contoured at 2 σ are shown in grey, and Fo-Fc maps contoured at 4 σ with positive and negative density are shown in green and red, respectively. Refined B-factor values in Å^2 are indicated for the different atoms.

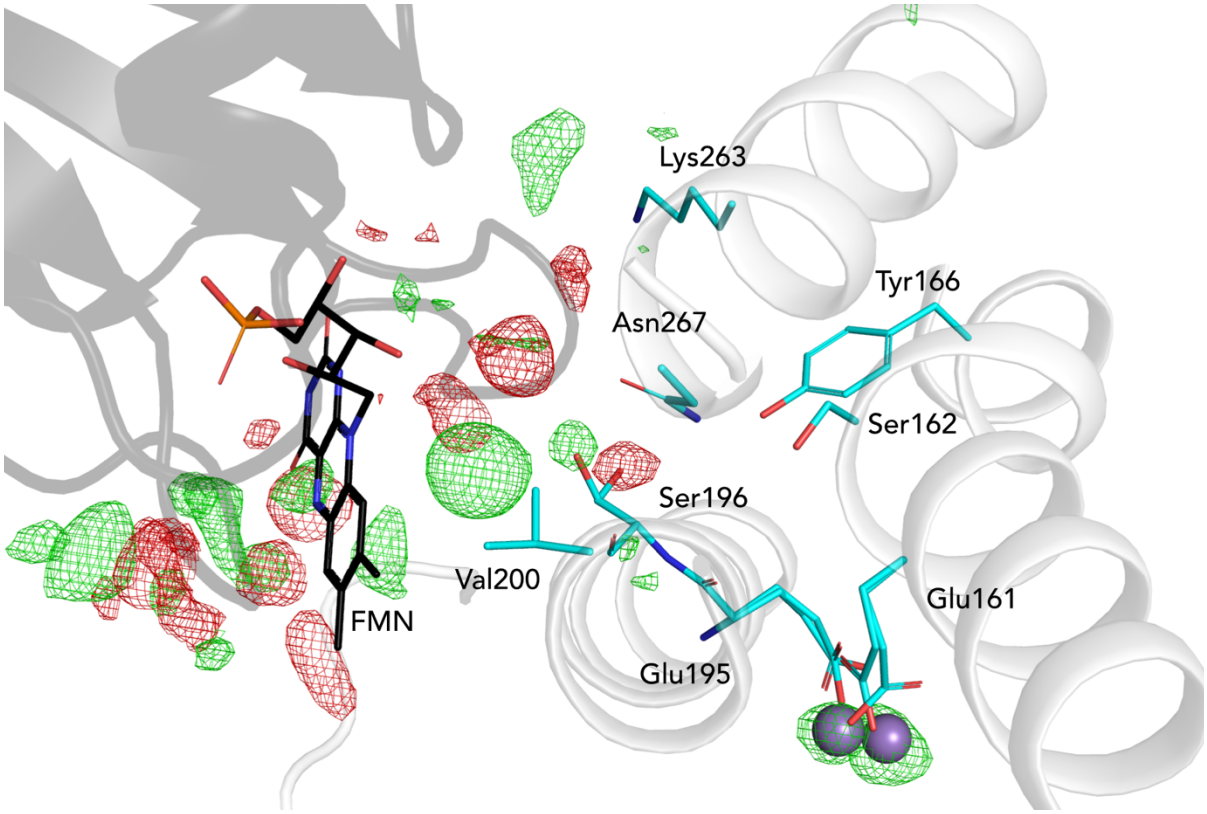

S 4 **Channel between R2b and NrdI**. NrdI is represented in black and R2b in white. Residues lining the channel from FMN (black sticks) towards the di-manganese site (purple spheres) are shown as sticks in cyan. The Fo(ox)-Fo(hq) map is shown as mesh and contoured at 4.5 σ with green as positive and red as negative density. The observed unknow molecule is in the vicinity of the channel. Changes around the FMN do not protrude towards the metal site in R2b.

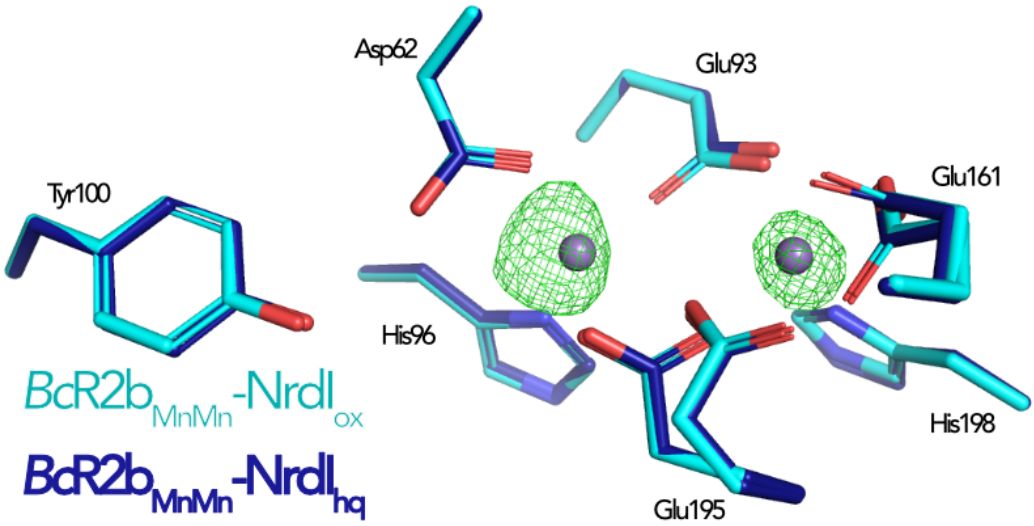

865

866 S 5 **Comparison of the active site in di-manganese *Bc*R2b$_{MnMn}$-NrdI structures.** The Fo(ox)-Fo(hq) map is

867 shown as mesh and contoured at 4.5 σ. The only observable change between the structures is the metal

868 occupancy.